DL^{3}M: A Vision-to-Language Framework for Expert-Level Medical Reasoning through Deep Learning and Large Language Models

Md. Najib Hasan[1], Imran Ahmad[2], Sourav Basak Shuvo[3], Md. Mahadi Hasan Ankon[4], Sunanda Das[5], Nazmul Siddique[6], Hui Wang[7]

[1]Dept. SoC, Wichita State University, USA [2]Dept. School of Business, Wichita State University, USA
[3]Dept. of BME, KUET, Bangladesh [4]Dept. of CSE, KUET, Bangladesh
[5]Dept. of EECS, University of Arkansas [5]Dept. SoC, Eng. and Intel. Sys., Ulster University, UK
[6]School of EEECS, Queen's University Belfast, UK

arXiv:2512.13742v1 [cs.CV] 14 Dec 2025

Abstract

Medical image classifiers detect gastrointestinal diseases well, but they do not explain their decisions. Large language models can generate clinical text, yet they struggle with visual reasoning and often produce unstable or incorrect explanations. This leaves a gap between what a model sees and the type of reasoning a clinician expects. We introduce a framework that links image classification with structured clinical reasoning. A new hybrid model, MobileCoAtNet, is designed for endoscopic images and achieves high accuracy across eight stomach-related classes. Its outputs are then used to drive reasoning by several LLMs. To judge this reasoning, we build two expert-verified benchmarks covering causes, symptoms, treatment, lifestyle, and follow-up care. Thirty-two LLMs are evaluated against these gold standards. Strong classification improves the quality of their explanations, but none of the models reach human-level stability. Even the best LLMs change their reasoning when prompts vary. Our study shows that combining DL with LLMs can produce useful clinical narratives, but current LLMs remain unreliable for high-stakes medical decisions. The framework provides a clearer view of their limits and a path for building safer reasoning systems. The complete source code and datasets used in this study are available at https://github.com/souravbasakshuvo/DL3M.

1 Introduction

The Gastrointestinal (GI) system is vital for digesting food and maintaining health through organs like the stomach and intestines. However, this system is susceptible to disruptive disorders like polyps, colon cancer, and ulcerative colitis, which can affect organs such as the stomach, intestines, liver, and pancreas (Ahamed et al., 2024a; Şener and Ergen, 2025). If left unmanaged, some of these abnormalities can ultimately develop into cancer (Wang et al., 2025).

GI cancers represent a major global health challenge, accounting for approximately 4.8 million new cases and 3.2 million deaths in 2022, which together constitute nearly one third of all cancer related mortalities worldwide (Ahamed et al., 2024b; Staff, 2020). A considerable proportion of this burden lies in Asia, with East Asia alone reporting 1,469,225 new gastrointestinal cancer cases and 837,360 deaths in the same year, corresponding to 43.1 percent and 41.7 percent of the global totals, respectively (Chong et al., 2024). Doctors use several tools to examine and treat problems in the GI tract. These include colonoscopy, upper GI endoscopy, capsule endoscopy, radiographic imaging, and lab tests (Kulinna-Cosentini et al., 2024). However, diagnosis results can vary depending on the doctor's experience, which makes the process unreliable at times. Reviewing thousands of endoscopic images manually is also a major challenge, increasing the chance of missed diagnoses and delays in treatment (Xie et al., 2024; Fernandes et al., 2024), leading to conditions that can quickly progress into serious stages.

Endoscopic image analysis faces issues like heavy visual clutter, inconsistent lighting, overlapping tissue patterns, and unwanted artifacts (Wang et al., 2026; Hayat et al., 2025; Lin et al., 2024). Many diseases from different categories appear very similar, while the same disease can show different patterns in different patients. These factors reduce the accuracy of diagnosis (Zeng et al., 2024). The quality and detail of the captured endoscopic images also play a big role in whether a condition is correctly identified (Tomazic et al., 2021; McCafferty et al., 2018).

To improve diagnosis, several classification methods have been developed. These methods can classify images with better precision, helping doctors in detecting and diagnosing conditions more efficiently. Moreover, in underdeveloped and developing countries ,the doctor-to-patient ratio is

quite iimbalanced (Karan et al., 2021; Nawaz et al., 2025). As a result, doctors can not pay enough attention to low-risk medical conditions like stomach infections (naming of the disease) (Su and Liu, 2025). This raise a serious concern to develop an automated system that could reduce the workload of doctors (Gumilar et al., 2025; Ghorbian et al., 2025), average patient waiting time, and increase reliability (He et al., 2020; Yilmaz et al., 2024). The automated system should be able to collect, process, classify, and give reasoning for normal and abnormal findings to serve as a reliable medical tool (El Ogri et al., 2026). This would lead to faster, more accurate treatment decisions and help lower the number of deaths from GI diseases worldwide (John et al., 2024).

Over the past few years, a significant number of studies have been conducted on the classification of stomach infections using deep learning (Naseem et al., 2025; Siddiqui et al., 2025; Shuvo and Chowdhury, 2024). Several studies have explored the usability of large language models (LLMs) in medical domain for clinical question answering, report generation, and decision support. In some studies, LLMs have been evaluated for medical text understanding, diagnosis, and prediction from textual data. However, none of these studies combined image-based disease classification with reasoning tasks.

In our experiment, we explore the effectiveness of LLMs for deep learning model assisted reasoning generation. This approach is necessary as LLMs are text-based models and cannot directly interpret the visual data, such as endoscopic images. If we send image in a different format (like a NumPy array or a matrix) to a text-based LLM using prompt, there will be a large information gap and the model will fail to extract important features from that image. Our solution incorporates DL models to first detect the disease from images, and then uses LLMs to provide appropriate reasoning and initial clinical advice on the diagnosis. We developed a benchmark dataset to evaluate and select best performing LLMs for medical reasoning.

Therefore, to summarize the research insights, this study focuses on the following Research Questions (RQs):

- **RQ1:** How does classification influence LLMs?
- **RQ2:** How effective are LLMs in clinical reasoning when DL is used as classifier?
- **RQ3:** Can LLMs simulate human-like expertise for reasoning?

Most of the existing studies either focus on classifying medical images without explaining the results or evaluate LLMs only through text-based tasks. As a result, there is still a gap between what is seen in the image and the kind of clinical reasoning needed to support real medical decisions. To bridge these gaps, our study introduces a unified framework that links image-based disease detection with LLM-driven reasoning and provides a systematic way to evaluate their combined performance. The notable contributions of this research are as follows:

- We introduce a deep-learning–assisted LLM framework that produces richer and more reliable clinical reasoning than existing single-model approaches.
- We propose a structured model selection strategy that pairs deep learning models for medical image classification with appropriate LLMs for clinical reasoning.
- We develop MobileCoAtNet, a lightweight yet powerful hybrid deep learning architecture tailored for medical image classification. This combine multi-level convolutional feature fusion with transformer-based contextual modeling.
- We present the first open benchmarking platform designed to evaluate LLM reasoning quality driven by deep learning model outputs. The taxonomy organizes LLMs into three categories, human-like, adaptive, and objective clinical reasoners-providing a transparent way to compare their strengths.

The remainder of this paper is organized as follows. section 2 reviews the existing literature relevant to this study. The problem definition and objectives are presented in section 3. The proposed methodology, including data collection, feature extraction, and model design, is detailed in section 4. The experimental setup, including the dataset and implementation details, is described in section 5. The results and key findings, along with comparisons to prior work, are reported in section 6. A detailed discussion of the results is provided in section 7. The conclusions are drawn in section 8, while the limitations of the study and possible future directions are outlined in section 9.

2 Related Work

2.1 Deep Learning based Classification

Deep Learning (DL), particularly Convolutional Neural Networks (CNNs), has established a dominant position in medical image classification and analysis(Li et al., 2024; Fahim et al., 2025; Ahmad and Alqurashi, 2024). These models have significantly enhanced diagnostic precision by automating the detection of intricate visual features that are traditionally analyzed manually. However, a systematic review of the literature reveals that while these architectures excel at feature extraction and classification accuracy, they consistently operate as black box systems. They maintain a heavy reliance on statistical feature correlation rather than explicit diagnostic reasoning.

Early research concentrated on feature fusion and optimization within controlled or standard (Hasan et al., 2025b,c). Naz et al. (Naz et al., 2021) developed a dual-pipeline system combining image enhancement with parallel Inception V3 and LBP feature extraction. By selecting optimal features via Shannon Entropy for an Ensemble Learning Classifier, this method reached 99.80% accuracy on a 3-class private dataset. Performance fell to 87.80% on the public 8-class Kvasir dataset, indicating that generalization is restricted as class complexity grows. To improve efficiency in these standard environments, Khan et al. (Khan et al., 2025) proposed a network-level fusion of a Sparse Convolutional DenseNet201 with Self-Attention and a CNN-GRU hybrid. Their Shallow Wide Neural Network, optimized via an Entropy-controlled Marine Predators Algorithm, attained 99.60% accuracy across 7 classes (Kvasir-V1) and 95.10% across 8 classes (Kvasir-V2). Khan et al. (Khan et al., 2024) also applied a parallel strategy using Darknet-53 and Xception streams optimized by the Binary Dragonfly Algorithm. The concatenated vector was then classified with an Ensemble Subspace k-Nearest Neighbors classifier. This yielded 98.25% accuracy on the 8-class Kvasir-V2, although the ESKNN classifier required longer training times.

Other studies aimed to improve the 8-class Kvasir benchmark by adding localization or attention mechanisms to generate more interpretable features. Alhajlah et al. (Alhajlah et al., 2023) presented a multi-stage pipeline using Mask R-CNN to localize infections before feature extraction with fine-tuned ResNet-50 and ResNet-152 models. This resulted in 96.43% accuracy, but the sequential steps added substantial computational overhead. Alternatively, Demirbaş et al. (Demirbaş et al., 2024) proposed the Spatial-Attention ConvMixer, which integrated a Spatial Attention Mechanism to highlight specific regions. The model achieved 93.37% accuracy on the 8-class Kvasir dataset. This was only a slight improvement over the baseline ConvMixer at 92.48%, suggesting that attention mechanisms alone are insufficient for major performance gains without deeper reasoning capabilities.

Limitations in statistical DL approaches are evident when scaling to datasets with 23 or more classes. Rubab et al. (Rubab et al., 2025) replaced pooling in ResNet architectures with an Entropic Field Propagation layer, optimized by a Newton-Raphson Marine Predator algorithm. Although it reached 99.0% accuracy on the 8-class Kvasir V1, performance fell to 82.7% on the complex 23-class Hyperkvasir dataset. Haseeb et al. (Haseeb et al., 2023) applied a parallel-stream Nasnetmobile with a custom Stacked Auto-Encoder to the same 23-class dataset. The resulting 93.80% accuracy proved slightly lower than the single-stream Nasnetmobile at 93.9%, indicating the autoencoder added complexity without benefit. Ahamed et al. (Ahamed et al., 2024c) also designed a lightweight Parallel Depthwise Separable CNN optimized with the Pearson Correlation Coefficient. When applied to the 27-class GastroVision dataset, the model achieved 87.75% accuracy. Authors attributed this result to severe class imbalance and the difficulty DL models face in distinguishing numerous classes without a robust reasoning framework.

While the reviewed literature confirms that DL models excel at image classification, they fundamentally lack reasoning capabilities. Across studies ranging from simple 8-class problems to complex 27-class datasets, no methodology successfully incorporated mechanisms to explain the logical basis of a diagnosis. The current state-of-the-art relies strictly on statistical pixel correlations, operating effectively as a black box. However, this dependence limits accuracy when scaling to high-dimensional data, as statistical features alone struggle to distinguish between numerous complex categories. This highlights a critical gap: the need to move beyond simple classification toward reasoning-based architectures that offer the logical transparency required for clinical practice.

2.2 LLM-based Classification and Reasoning

Recent advances in multi-modal LLMs have expanded their capabilities to integrate textual and visual medical data, enhancing diagnostic reasoning. Agbareia et al. (Agbareia et al., 2025) evaluated the visual-textual integration mechanism in GPT-4o and Claude Sonnet 3.5 against physicians on 120 clinical vignettes presented in text-only and text + image formats for medical diagnosis. Using a dataset from the OPENI database and recent NEJM challenges, LLMs outperformed physicians in text-only scenarios where GPT-4o achieved 70.8% accuracy, Claude Sonnet 3.5 achieved 59.5% accuracy, while physicians achieved 39.5% accuracy. With the addition of images, all groups showed improved accuracy, but physicians demonstrated the largest accuracy gain (from 39.3% to 78.8%), significantly exceeding the LLMs' gains, where in the case of GPT-4o, accuracy increased from 13.7% to 84.5%; in Claude Sonnet 3.5, accuracy increased from 7.8% to 67.3%. Both models confirmed genuine integration of visual data by changing their explanations in 45-60% of cases when images were provided. The core limitation identified is the LLMs' smaller relative gain, suggesting limited visual reasoning capacity, an open-evaluation process (Hasan et al., 2025a) and a continued heavy reliance on text-based knowledge compared to human clinicians. Similarly, Kaneyasu et al. (Kaneyasu et al., 2025) investigated the image-recognition capabilities of five multimodal LLMs on the Japanese National Examination for Dental Hygienists. The methodology used a zero-shot (Sarkar et al., 2025) evaluation on 213 multiple-choice questions (74 text-only, 139 visually-based). Gemini 2.5 Pro Experimental achieved the highest overall accuracy score of 85.0%. Critically, for the visually-based questions, Gemini 2.5 was significantly superior at 82.0% accuracy, outperforming other models, which averaged 70-73% , suggesting that advanced image understanding is a new differentiator among LLMs. This highlighted progress in vision-language integration for clinical images. The principal limitation is the LLMs' imperfect accuracy (Gemini 2.5 still missed 15% of the questions), resulting in an error rate too high for unsupervised use in high-stakes settings, compounded by potential linguistic and training-data biases (Das et al., 2024) and the tendency toward hallucinations (Das et al., 2025).

Rewthamrongsris et al. (Rewthamrongsris et al., 2025) evaluated seven multimodal LLMs in the image-based diagnostic detection and differential diagnosis of Oral Lichen Planus (OLP), comparing them against specialized Convolutional Neural Networks (CNNs). The methodology tested the LLMs using a 1,142-image dataset across three designs: zero-shot recognition, example-guided recognition (a prompt engineering strategy), and differential diagnosis generation. Example-guided prompting improved performance; Gemini 1.5 Flash achieved the highest 80.53% accuracy in the guided recognition task, while Claude 3.5 Sonnet excelled at ranking differential diagnoses. The core finding is a limitation: all LLMs were outperformed by the specialized CNN models for OLP detection. This discrepancy stems from LLMs being trained on publicly available data, which lacks sufficient domain-specific OLP-labeled examples, thereby limiting their single-task classification accuracy. The review asserts that LLMs possess powerful reasoning capabilities but are poor at classification. This suggests that when reasoning with image information, a combination of DL with LLM would be a better choice for improved reasoning in the medical imaging domain.

3 Problem Statement

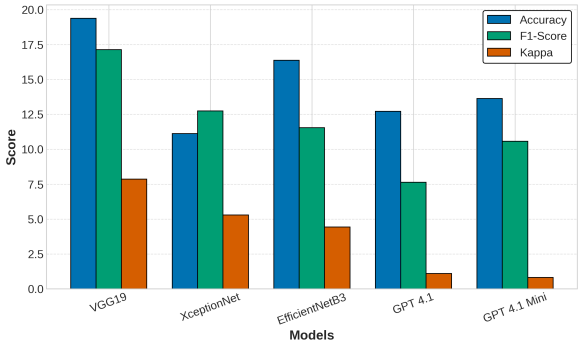

Figure 1: Performance comparison for zero-shot multi-label medical image classification of DL and LLMs.

Disease diagnosis and clinical reasoning have become a crucial problem for generic diseases, such as stomach infections. LLM can be an option to automate the whole system. Before blindly integrating LLM for a sensitive domain of medical diagnosis, we initially experimented to investigate their performance on diagnosis and classification tasks. We select the best LLMs after 0-shot MSR (Zero-shot Multi Step Reasoning) and benchmark their performance for the classification task on the Kvasir2 (Stomach disease) dataset containing eight

different classes. In our experiment, we have used a prompting strategy P and sent the image I and a set of disease classes S_d as input. In the prompt, we include the directives and ask the model L to predict the best-suited disease class Y for the given image.

$$Y = L\big(P(I, S_d)\big) \tag{1}$$

From this initial experiment and comparing with zero-shot deep learning models for the classification task, we find that LLMs are not sufficiently capable for zero-shot disease diagnosis, and it can further impact clinical reasoning generation, refer to Figure 1. To overcome the pitfalls of blindly relying on LLMs, we develop a hybrid pipeline where a fine-tuned hybrid DL model M will work for disease classification C (diagnosis), and LLMs L will work for clinical reasoning generation R.

$$R, C = L\big(M(I, S_d)\big) \tag{2}$$

4 Methodology

To enhance reasoning in LLM, prior classification of images is proven to be useful. Therefore, classification of images, particularly medical images in this research, is performed using DL models prior to their use in LLM. A set of 26 DL models was chosen for investigation, which underwent a zero-shot task on stomach infection endoscopy images. A subset is then selected based on the zero-shot task. Since pretrained DL models often fail to generalize effectively to unseen domains or tasks, it was necessary to fine-tune all the selected models along with the proposed hybrid model, MobileCoAtNet.

4.1 Classification using Deep Learning

For fine-tuning the DL models, the image dataset was divided into training, validation, and testing subsets with a ratio of 70:20:10. During the fine-tuning process, all pretrained layers of the selected models were frozen to preserve their learned representations, while only the output layers were trained to adapt to the new task.

(i) Proposed MobileCoAtNet Architecture: On top of the eight pretrained models chosen using zero-shot learning, we introduced a new architecture named MobileCoAtNet. The proposed architecture (see Figure 2a) comprises two branches: an upper branch and a lower branch. These branches can incorporate various combinations of base models to construct the complete proposed framework. Three base models were considered: ViT, ResNet50, and XceptionNet based on their performance. In the final configuration, the upper branch employs XceptionNet, while the lower branch utilizes ResNet50.

Preprocessed images with a size of $128 \times 128 \times 3$ were fed into pretrained XceptionNet, ResNet50, and ViT models, which were utilized without their top layers to preserve general features while enabling domain adaptation for endoscopic analysis. From each branch, three layers were selected to extract features that were then passed through separate transition_block modules using a consistent filter size of 512. Structurally, each transition_block consisted of a loop containing a separable convolution layer that is activated only when the first dimension is greater than 4.

Subsequently, outputs from six transition blocks with a shape of $4 \times 4 \times 512$ were processed by six LSTMs to produce vectors of size 1024. These outputs were reshaped into $4 \times 4 \times 256$ and concatenated with the corresponding transition_block features to result in a combined shape of $4 \times 4 \times 768$.

The combined features from each branch were passed into the mobile_bottleneck producing an output with a dimension $4 \times 4 \times 512$, which is repeated for all four feature sets. The outputs of each branch's mobile_bottleneck were concatenated with the corresponding transition_block outputs from the opposite branch, producing a fused feature map of $4 \times 4 \times 1024$.

The fused features were processed through four CoATNet modules. In each branch, outputs from two modules were concatenated and refined via a transition_block to form a $4 \times 4 \times 512$ feature map. The resulting transition_block outputs were then merged to produce a final $4 \times 4 \times 1024$ feature map.

The aggregated output was fused with the concatenated features from the final mobile_bottleneck of each branch, producing a $4 \times 4 \times 2048$ feature map. This was flattened into A with 32,768 elements, while the outputs of all six LSTM units were combined into B with 6,144 features.

Vectors A and B were concatenated to form C with 38,912 features. A sequence of Dense and Dropout layers reduced C to a vector D of 2,048 features. D was then merged with the ViT output vector E (1,000 features) to produce the final

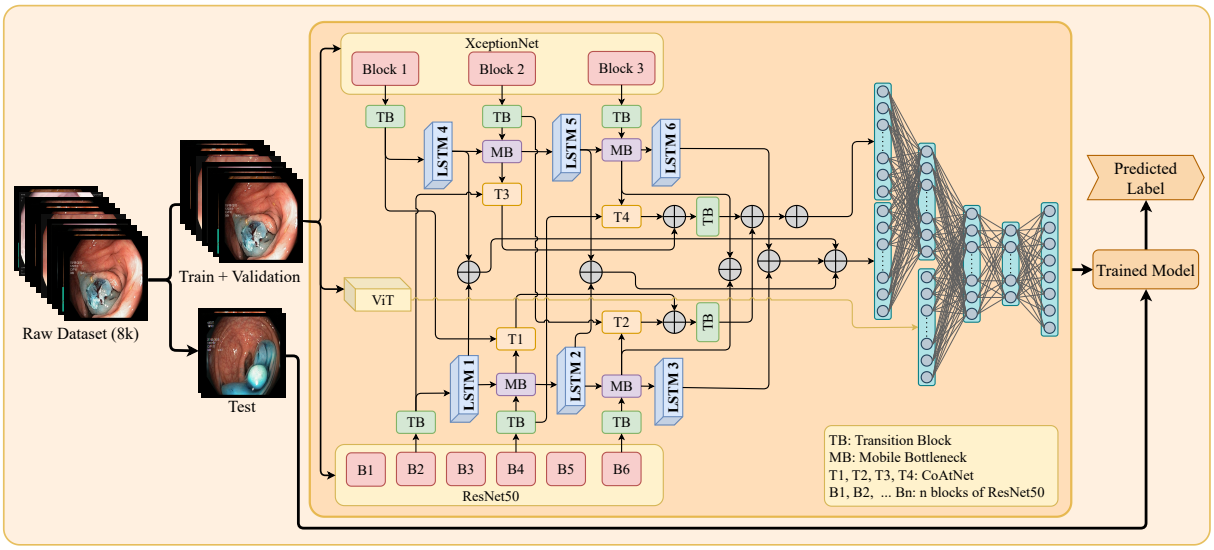

(a) The working principle of MobileCoATNet

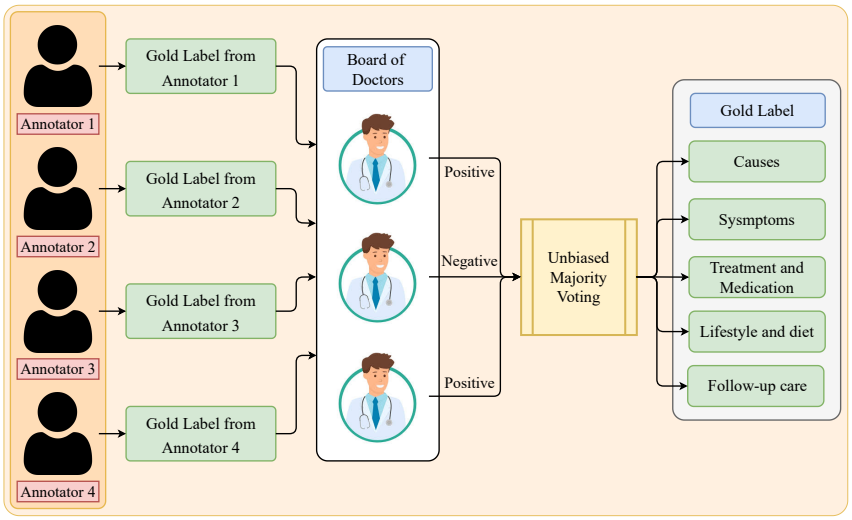

(b) A framework to generate human annotation for the benchmarks.

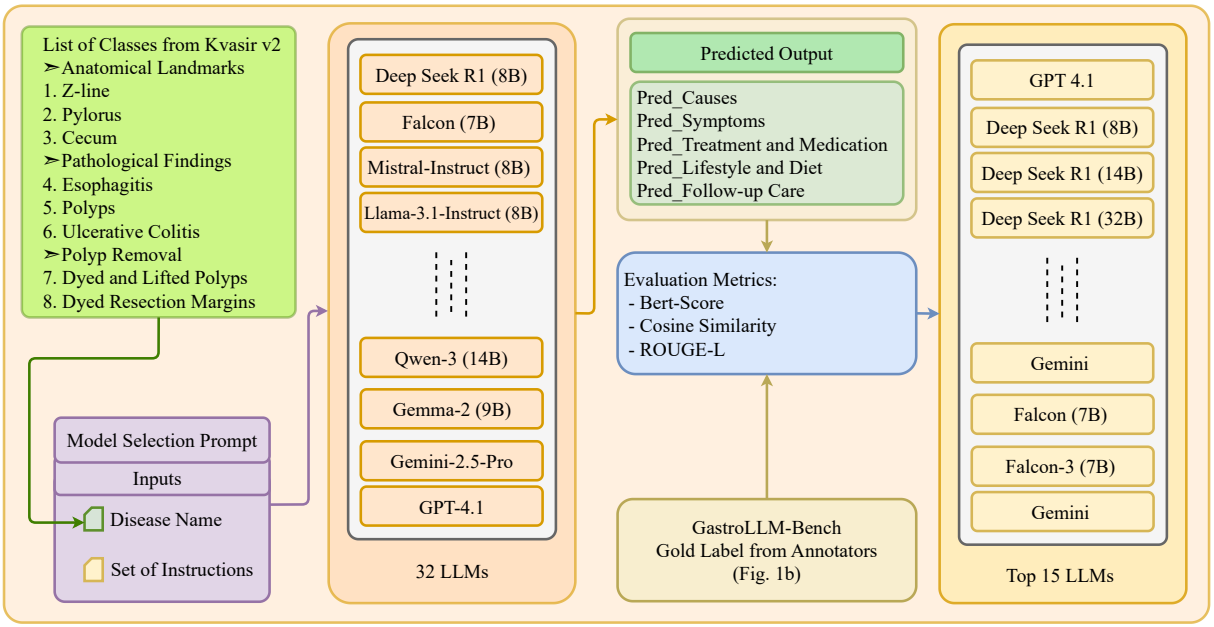

(c) Benchmarking for initital LLM selection.

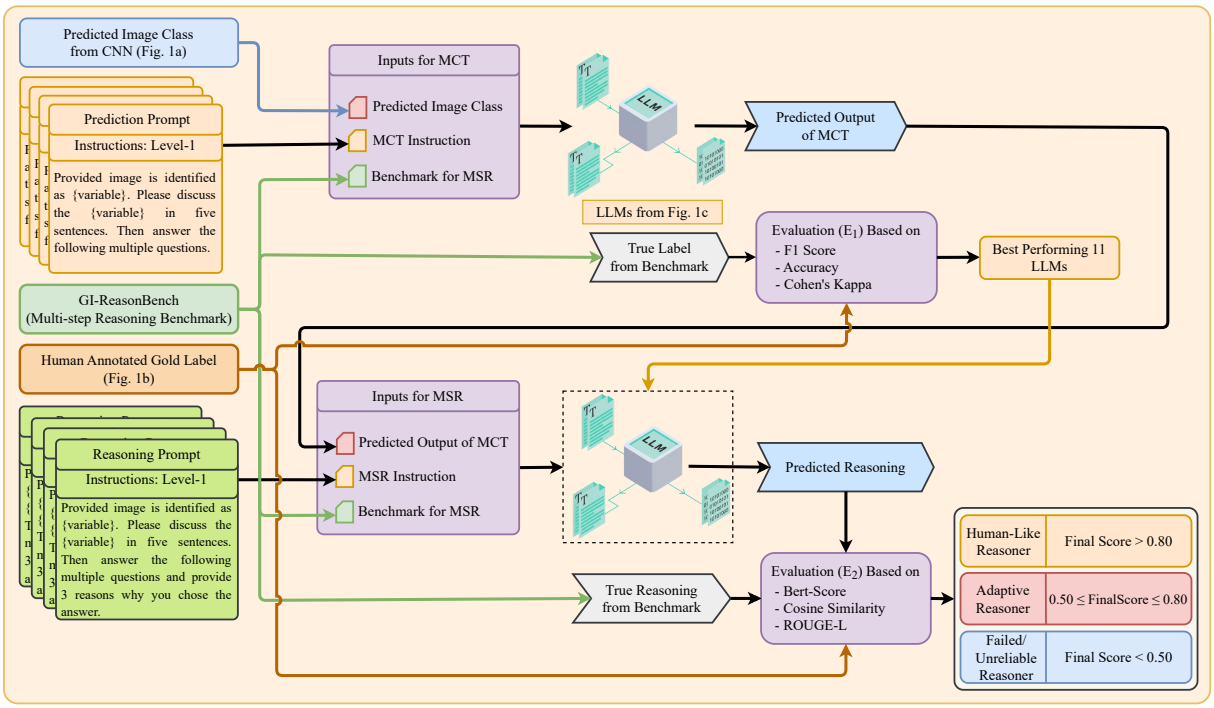

(d) DL-based multi-step reasoning using LLMs

Figure 2: Overall methodology: (a) Medical image classification using MobileCoAtNet to diagnose the disease level, (b) A multi-step majority voting-based benchmark annotation pipeline for gold-label generation, (c) A pipeline for zero-shot-based initial LLM selection for clinical reasoning tasks, and (d) The image classified from a DL model and the predicted label is sent to an LLM for multi-step clinical reasoning generation.

combined vector F with 3,048 features. Multiple Dense and Dropout layers were applied to F to generate the predicted output. The classification information was then fed to LLMs through prompt engineering to assess the reasoning ability of the models.

4.2 Reasoning using LLM

As our objective is to evaluate LLMs for reasoning and assess their generalizability within the GI domain, we selected a range of models from top-tier LLM families. For this experiment, we included models from OpenAI, Gemini, LLaMA, DeepSeek, Qwen, and Falcon, encompassing a total of 32 LLMs, of which 19 were open-source and 13 were proprietary. Model selection began with the smallest parameter versions within each family. If a given model failed to achieve satisfactory performance, a larger variant from the same family was subsequently evaluated.

From this initial screening, the 15 best-performing LLMs were identified using a zero-shot prompting approach (see reference to the prompt). This benchmarking phase ensured that only models demonstrating a baseline level of knowledge related to stomach infection were retained. Finally, a two-stage evaluation framework was established to categorize LLMs based on their performance in reasoning and classification tasks. The complete experimental benchmark, referred to as [Gastro-reason-bench], was developed to support this evaluation process.

(i) Benchmark Design: The benchmark design begins with the development of two comprehensive "Gold Label" benchmarks focused on the gastrointestinal (GI) tract: one for model selection and the other for multi-step reasoning. The process begins with an extensive review of research papers, official health organization websites, and other credible medical sources to ensure accurate initial annotations. For LLM evaluation, the original eight classes were consolidated into five to align with common clinical decision categories. The three anatomical landmarks (Z line, Pylorus, and Cecum) were merged into the Healthy Class, while the two polyp removal categories (Dyed and Lifted Polyps and Dyed Resection Margins) were combined as Removal of Lesions. The remaining pathological classes (Esophagitis, Polyps, and Ulcerative Colitis) were retained as separate labels. The final

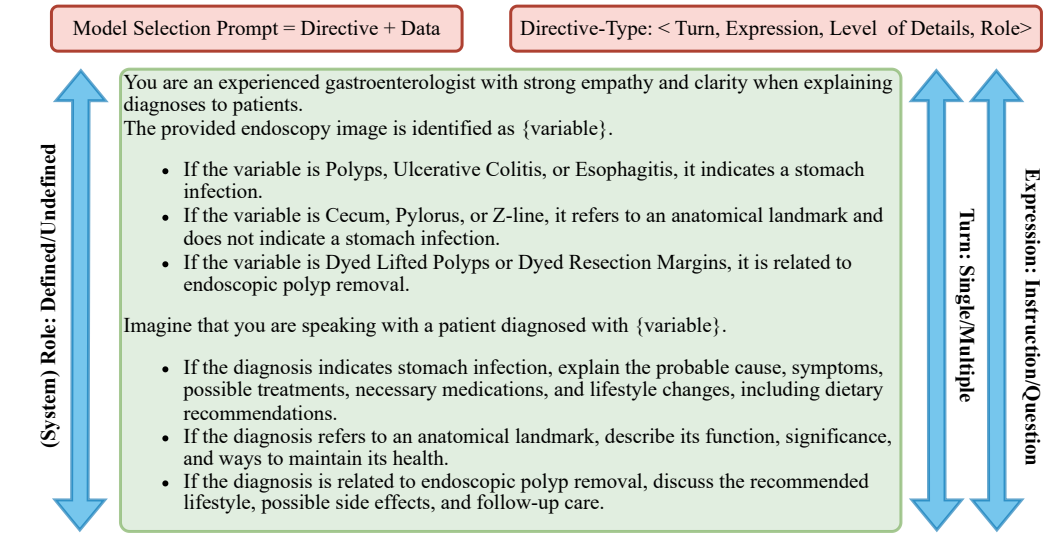

(a) Prompt for zero-shot-based initial LLM selection.

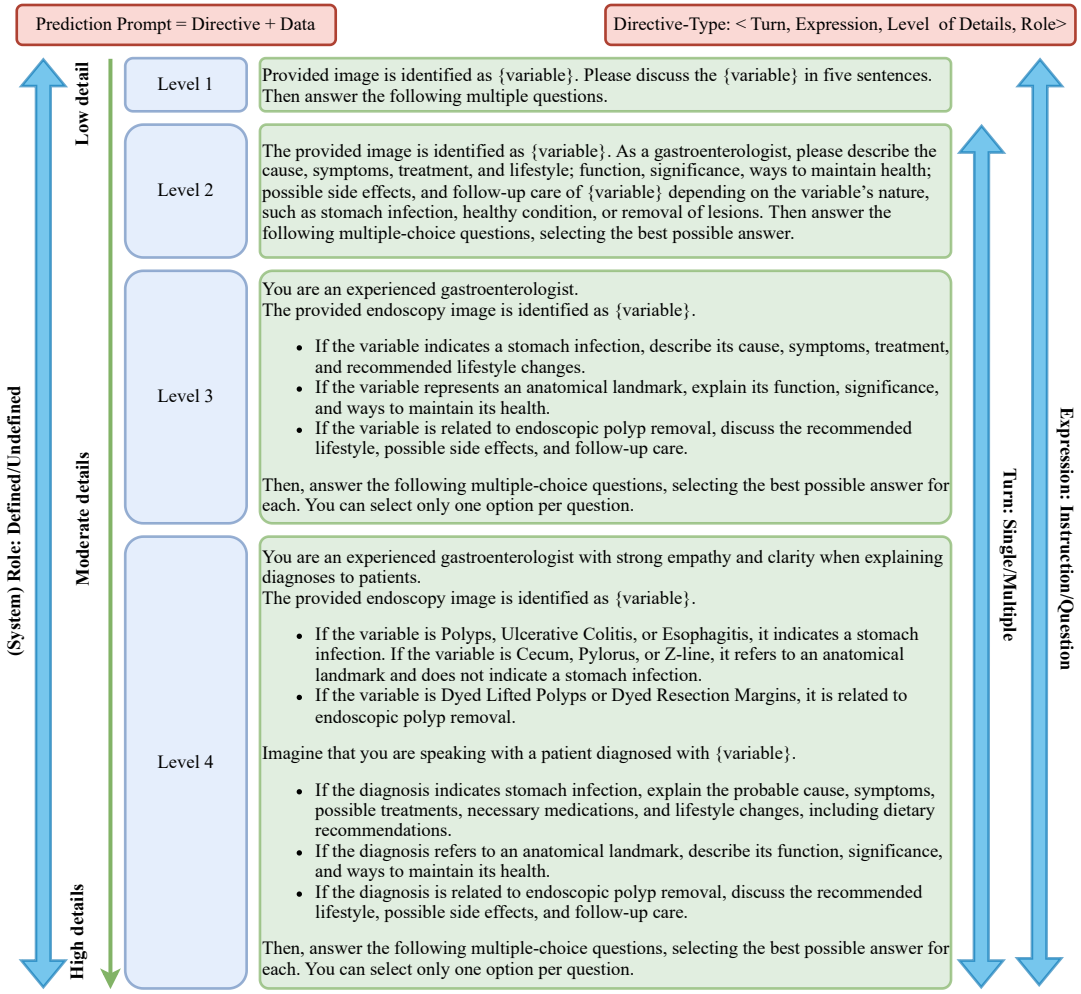

(b) Prompt for LLM-based multiple-choice task.

label set consisted of Healthy, Esophagitis, Polyps, Ulcerative Colitis, and Removal of Lesions.

Detailed annotations were created under five medical categories: 'Causes', 'Symptoms', 'Treatment' and Medication', 'Lifestyle and Diet', and 'Follow-up Care'. These annotations were independently prepared by five human experts, identified as Gold Label from "Annotator 1" through "Annotator 5." The annotated data were then reviewed and refined through majority voting with a "Board

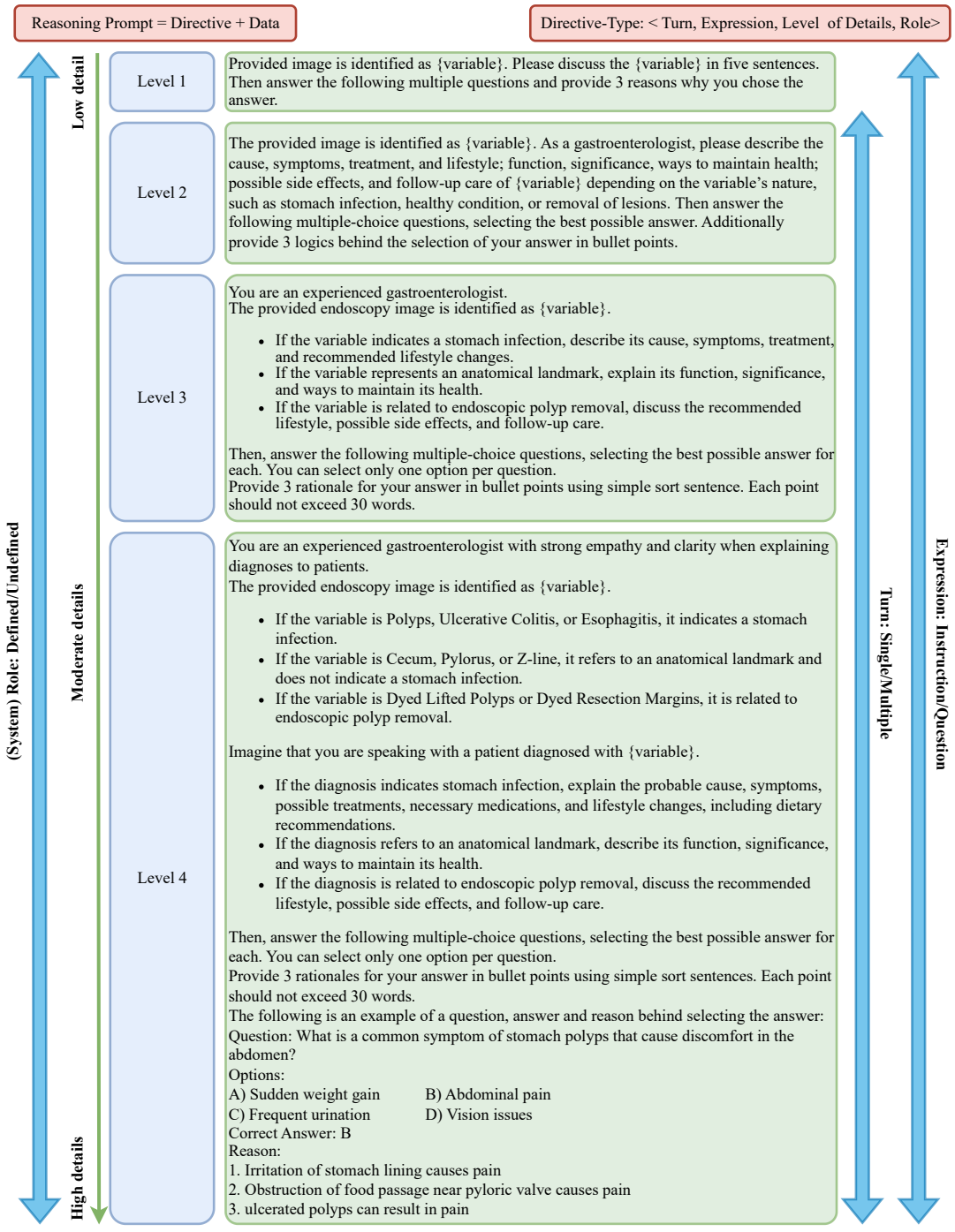

(c) Prompt for LLM-based reasoning generation.

Figure 3: Three different prompts, (a), (b), and (c), have been used for three different tasks. For each task, we have used a taxonomy of prompts, where four different levels of prompts are used with varying levels of directives.

of Doctors" to ensure medical accuracy and consistency, resulting in the final version of the "Gold Label" benchmarks.

Benchmark-1, GastroLLM-Bench, consists of information to evaluate 32 LLM models on a zero-shot prompt (Figure 3a). The information gathered consists of all possible causes, symptoms, treatment and medication, lifestyle and diet, and follow-up care. Benchmark-2 was created with multiple-choice questions across the 5 categories (Causes, Symptoms, Treatment and Medication, Lifestyle and Diet, and Follow-up Care) with reasons behind the right answers. The benchmark-2, GI-ReasonBench, consists of 375 questions, 100 questions each for the disease classes: Polyps, Ulcerative Colitis, and Esophagitis. Additionally,

there were 25 questions related to healthy anatomical classes such as the Cecum, Pylorus, and Z-line. These questions focused on the importance of these anatomical structures and lifestyle practices for maintaining a healthy stomach. Lastly, 50 questions were designed for the removal of lesions, including Dyed Lifted Polyps and Dyed Resection Margins, with questions regarding their purpose, potential side effects, medical follow-up, and associated lifestyle and dietary habits.

4.3 Evaluation Strategy of LLM reasoning

A systematic evaluation of LLMs was carried out to measure their effectiveness in handling disease-related queries in the gastrointestinal domain. The evaluation framework included three main components - (i) LLM selection, (ii) assessment of multi-step reasoning, and (iii) prompt strategies.

(i) LLM Selection: A zero-shot prompting strategy was used to develop a model selection prompt that guides LLMs in generating relevant responses from the Kvasir-v2 dataset. As shown in Figure 3a, the prompt provides each class name together with a set of queries. This ensures that every model consistently interprets the dataset's categories — such as anatomical landmarks, stomach infection, and endoscopic polyp removal—and generates responses aligned with clinical reasoning. The prompt was applied to thirty-two LLMs from major LLM families, including OpenAI, Gemini, Falcon, Mistral, and DeepSeek. Each model produced outputs for the defined categories, and these responses were compared against human annotated gold-output. Finally, three evaluation metrics—BERTScore, Cosine Similarity, and ROUGE-L were used to assess semantic accuracy, contextual relevance, and textual coherence. The top-performing models were then selected for multi-step reasoning.

(ii) Assessment of Multi-step Reasoning Performance: To investigate LLMs' knowledge depth and proper generalization, the best performing models were evaluated on Benchmark-2 for two different tasks - Multiple-choice task and Reasoning task.

(A) Multiple-choice Task: The selected models were evaluated using four prompt sets, including zero-shot and one-shot variants (Figure 3b). In this stage, each LLM received images that had already been classified by the DL model, along with their predicted labels. Based on the predicted class, the LLMs were prompted to provide specific information. For stomach infection classes, they were given multiple-choice queries covering causes, symptoms, treatment options, and lifestyle recommendations, and were asked to select the most suitable answer. For anatomical landmark classes, the queries focused on function, clinical significance, and strategies for maintaining overall health. For endoscopic polyp removal classes, the questions addressed lifestyle guidance, potential side effects, and recommended follow-up care. The outputs produced by the LLMs were compared with gold labels and evaluated using Accuracy, F1-score, and Cohen's Kappa. Based on these results, the best-performing models were selected for the reasoning task and used for further analysis.

(B) Reasoning Task: The top-performing models from the multiple-choice stage were then evaluated on the reasoning task. In this experiment, each LLM received several components through the prompt: a question–answer pair where the answer was generated by that same LLM, an endoscopic image with its predicted label, and an instruction to provide three justifications explaining why the predicted answer aligns with the given question. The full prompts are shown in Figure 3. The generated reasoning was compared with human-produced gold reasoning using BERTScore, cosine similarity, and ROUGE-L to identify the best-performing models.

(iii) Prompting Strategies: To investigate prompt sensitivity of LLMs, we developed four sets of prompts for each benchmark. Prompts one, two, and three were zero-shot prompts, while prompt four was a one-shot prompt. We structured the prompting sequence progressively, starting from general instructions and moving toward more specific guidance, with the final prompt including an illustrative example. Figure 3 presents an example from the benchmark.

5 Experimental Setup

5.1 Dataset Description

In this study, the training and evaluation of DL models were performed using the Kvasir-V2 dataset (Pogorelov et al., 2017). It is a well-curated collection of 8,000 high-resolution gastrointestinal endoscopy images specifically designed for research and benchmarking, balanced equally across eight distinct classes. This dataset, originating from Vestre Viken Health Trust in Norway, encompasses three anatomical landmarks (Z-line, Pylorus, and

Table 1: The set of performance metrics used to evaluate DL-based classification and LLM-based multi-step reasoning generation.

Metric	Formula
Accuracy	$\text{ACC} = \frac{\text{TP}+\text{TN}}{\text{TP}+\text{TN}+\text{FP}+\text{FN}}$
Loss	$L = \text{Loss}(y, \hat{y})$
Precision	$\text{PPV} = \frac{\sum_k \text{TP}_k}{\sum_k (\text{TP}_k + \text{FP}_k)}$
Sensitivity	$\text{SN} = \frac{\sum_k \text{TP}_k}{\sum_k (\text{TP}_k + \text{FN}_k)}$
Specificity	$\text{SP} = \frac{\sum_k \text{TN}_k}{\sum_k (\text{TN}_k + \text{FP}_k)}$
F1-Score	$F_1 = \frac{2 \times \text{PPV} \times \text{SN}}{\text{PPV} + \text{SN}}$
Cohen's Kappa	$\kappa = \frac{P_o - P_e}{1 - P_e}$
	$P_o = \text{ACC}$
	$P_e = \sum_{k=1}^{n} \frac{(\text{TP}_k + \text{FP}_k) \cdot (\text{TP}_k + \text{FN}_k)}{(\text{TP}_k + \text{TN}_k + \text{FP}_k + \text{FN}_k)^2}$
BERT-Score	$\text{BS} = \frac{1}{N} \sum_{i=1}^{N} \max_j \ \text{sim}(e_i^{ref}, e_j^{pred})$
ROUGE-L	$\text{ROUGE-L} = \frac{2 \times \text{LCS}(y, \hat{y})}{\lvert y \rvert + \lvert \hat{y} \rvert}$
Cosine Similarity	$\text{CosSim} = \frac{\vec{y} \cdot \vec{\hat{y}}}{\lVert \vec{y} \rVert \ \lVert \vec{\hat{y}} \rVert}$

Cecum), three pathological findings (Esophagitis, Polyps, and Ulcerative Colitis), and two classes related to polyp removal procedures (Dyed and Lifted Polyps and Dyed Resection Margins). All images, ranging in resolution from 720 × 576 to 1920 × 1072 pixels, were captured using advanced endoscopic equipment and subsequently verified by experienced gastroenterologists to ensure high clinical accuracy and ground truth reliability. The dataset provides a robust foundation for developing and benchmarking automated systems for gastrointestinal disease analysis.

5.2 Deep Learning Models

MobileCoAtNet comprises three main pretrained models XceptionNet (Chollet, 2017a), ResNet50 (He et al., 2016a), and ViT (Dosovitskiy et al., 2021a). Also the bottleneck of a lightweight model, MobileNetV2, and LSTM blocks/units are used in this study.

5.3 Large Language Models

Thirty-two LLMs from six families were evaluated: OpenAI (GPT-4, GPT-3.5), Gemini (Gemini 1, Gemini 1.5), LLaMA (LLaMA 2-7B), DeepSeek (DeepSeek R1), Qwen (Qwen-7B), and Falcon (Falcon-7B, Falcon-40B). On the other hand, closed source models are used since they are trained on huge parameters with improved performance (Kumar et al., 2024).

Table 2: Hyperparameters used for DL-based classification and LLM-based multi-step reasoning generation.

Category	Hyperparameter	Value
CNN (MobileCoAtNet)	Input size	$128 \times 128 \times 3$
	Patience	20
	Batch size	128
	Metrics	Accuracy
	Early stopping	True
	Loss	Sparse categorical cross-entropy
	Monitor	Val_accuracy
	Optimizer	Adamax
	Mode	Max
Open-source LLMs	Temperature	0.7
	Max tokens	50
	Top-p	1.0
	Do sample	True
	Context length	∼32K
Closed-source LLMs	Temperature	0.7
	Max tokens	50
	Context length	128K

5.4 Hyperparameters

This section outlines the specific hyperparameters utilized for training and inference across the different models employed in DL and LLMs. These settings, summarized in Table 2, were systematically chosen to ensure optimal performance, efficient training dynamics, and reproducibility of the results.

5.4.1 Hyperparameters for Deep Learning Models

The MobileCoAtNet model was trained using $128 \times 128 \times 3$ images and a batch size of 128. The Adamax optimizer was chosen, with accuracy selected as the performance metric. The 'sparse categorical cross-entropy' loss function was used, as it is suitable for multi-class tasks with integer labels. The loss for a single sample i is defined as:

$$L(y, \hat{y}) = -\log(\hat{y}_{i,y_i}) \tag{3}$$

Here, y_i is the true class index and $\hat{y}_{i,y_i}$ is the predicted probability for that class. To prevent overfitting, early stopping was applied. This monitored the validation accuracy in max mode and stopped the training if no improvement occurred for 20 consecutive epochs.

5.4.2 Hyperparameters for LLMs

The hyperparameters for the LLMs were configured to optimize their generative performance for the diagnostic tasks, with slight variations between open and closed-source models.

- **Open-source Models** For the open-source LLMs, a probabilistic sampling approach was enabled. The generation was controlled by a temperature of 0.7 to balance creativity and coherence, while top p was set to 1.0. These models operated with a context length of approximately 32K tokens (∼32K) and were limited to a Max token output of 50 new tokens.

- **Closed-source Models** The closed-source models were similarly configured with a temperature of 0.7 and a Max token limit of 50. These models, however, leveraged a significantly larger Context length of 128K tokens, allowing for the processing of more extensive input prompts.

5.5 Environment Setup

Both cloud and personal computing resources were used to develop and test the proposed hybrid deep-learning model for identifying stomach infection from gastrointestinal endoscopy images. The initial development took place on Kaggle, which provided each account with 15 GB of RAM, 170 GB of storage, and 30 GB of GPU memory. Preliminary model testing was conducted on Google Colab, where each account had 15 GB of GPU memory, 13 GB of RAM, and 10 GB of local storage. Additionally, the dataset was preprocessed on a personal computer with a Core i7 CPU, 32 GB of RAM, and an NVIDIA GPU.

5.6 Evaluation Strategy

To assess the efficacy of the proposed framework, a multi-stage evaluation protocol was established for both the deep learning visual classifiers and the large language reasoning models. The mathematical formulations for the quantitative metrics utilized throughout this study are summarized in Table 1.

(i) Best performing DL model selection: Initially, deep learning models were evaluated in a zero-shot setting, and the top eight were selected based on accuracy and F1-score. These eight pre-trained models, along with our proposed MobileCoAtNet, were then fine-tuned and evaluated using five-fold cross-validation. Their performance was assessed on a held-out test set using Test Accuracy, F1-Score, and Cohen's Kappa.

(ii) Best performing LLM selection: Initially, a range of models were selected from the most used LLM families based on three different categories of parameter size - (i) below 10 billion parameters, (ii) 10 to 50 billion parameters, and (iii) more than 50 billion parameters. These LLMs were initially evaluated on Benchmark-1 using zero-shot prompting and assessed using BERTScore, cosine similarity, and ROUGE-L metrics against a "Gold reasoning." The top-performing models were selected for a multi-step reasoning task, where they were evaluated using accuracy, F1-score, and Cohen's kappa.

(iii) Taxonomy of LLM Performance: To evaluate the models' ability to perform reasoning with minimal context, "Final Weighted Score" was computed, giving greater importance to prompts containing less specific information. For each prompt, a Composite Reasoning Score (CRS) was first calculated by averaging across all five classes and applying weighted metric importance.

$$\begin{aligned}\text{CRS}_\text{p} = w_1 \cdot \text{Avg\_Cosine}_p + w_2 \cdot \text{Avg\_BERT}_p \\ + w_3 \cdot \text{Avg\_Rouge}_p\end{aligned} \tag{4}$$

This combination was selected after performing an ablation study refer to Table 6. Cosine similarity was given the highest weight (w_1) to emphasize global semantic alignment and the overall direction of the reasoning. It operates on aggregated sentence embeddings, and it is particularly effective at capturing whether the generated rationale matches the underlying meaning of the gold reasoning, even when the wording differs. In contrast, BERTScore offers useful insight into token-level contextual accuracy but is weighted lower (w_2) because its token-wise alignment can penalize valid reasoning that uses different phrasing or vocabulary to express the same idea. Finally, ROUGE-L is included with the smallest weight (w_3), serving mainly to measure exact textual overlap.

The *Final Weighted Score* for each model was then obtained as a weighted sum of the prompt-specific CRS values:

$$\text{FinalScore} = \sum_{i=1}^{4} w_i \, \text{CRS}_i \tag{5}$$

We assign decreasing weights (0.4, 0.3, 0.2, 0.1) to the four levels of prompt Figure 3c because the earlier prompts (P1, P2) are designed to capture a model's general reasoning stability, while the

Table 3: Zero-shot medical image (endoscopic image of stomach disease) classification using DL models.

Model	Params (M)	Test Acc. (%)	F1-Score (%)	Precision (%)	Sensitivity (%)	Kappa (%)
VGG19 (Simonyan and Zisserman, 2015)	143.6	19.38	17.14	19.26	19.38	7.86
EfficientNetB3 (Tan and Le, 2019)	8.0	17.12	12.75	14.54	17.12	5.29
ResNet-50 (He et al., 2016b)	14.3	16.38	11.55	10.72	16.38	4.43
XceptionNet (Chollet, 2017b)	7.1	16.25	15.03	19.09	16.25	4.29
MobileNet V2 (Sandler et al., 2018)	55.8	16.12	10.79	13.70	16.12	4.14
VGG16 (Simonyan and Zisserman, 2015)	21.8	15.12	8.62	12.01	15.12	3.00
EfficientNetV2B0 (Tan and Le, 2021)	60.2	15.12	10.30	14.33	15.12	3.00
DenseNet-201 (Huang et al., 2017)	20.2	14.12	8.79	12.92	14.12	1.86
ViT-Base (Dosovitskiy et al., 2021b)	22.9	13.38	11.33	17.96	13.38	1.00
ResNet101V2 (He et al., 2016c)	44.6	13.25	10.64	12.52	13.25	0.86
ResNet-152V2 (He et al., 2016c)	60.3	12.88	7.54	9.21	12.88	0.43
Inception-ResNetV2 (Szegedy et al., 2017)	3.5	12.25	10.56	10.55	12.25	-0.29
EfficientNetV2B3 (Tan and Le, 2021)	14.5	12.25	6.87	7.75	12.25	-0.29
ResNet-101 (He et al., 2016b)	44.5	12.12	10.26	10.68	12.12	-0.43
EfficientNetB7 (Tan and Le, 2019)	66.4	12.12	3.92	8.79	12.12	-0.43
Inception V3 (Szegedy et al., 2016)	23.8	11.88	8.61	10.82	11.88	-0.71
ResNet-18 (He et al., 2016b)	11.7	11.75	9.47	20.93	11.75	-0.86
DenseNet-121 (Huang et al., 2017)	12.2	11.75	9.99	15.13	11.75	-0.86
EfficientNetB0 (Tan and Le, 2019)	5.3	11.12	9.09	10.70	11.12	-1.57
ResNet-152 (He et al., 2016b)	86.6	9.50	8.23	11.80	9.50	-3.43
MobileNetV3Large (Howard et al., 2019)	5.4	9.25	8.92	12.01	9.25	-3.71
Inception V4 (Szegedy et al., 2017)	42.7	8.88	6.99	15.35	8.88	-4.14
DenseNet-169 (Huang et al., 2017)	25.6	8.75	8.65	19.46	8.75	-4.29
ResNet-34 (He et al., 2016b)	138.4	8.12	6.49	10.20	8.12	-5.00
ResNet50v2 (He et al., 2016c)	25.6	8.12	5.25	5.93	8.12	-5.00
MobileNetV3Small (Howard et al., 2019)	2.5	7.38	4.82	3.74	7.38	-5.86

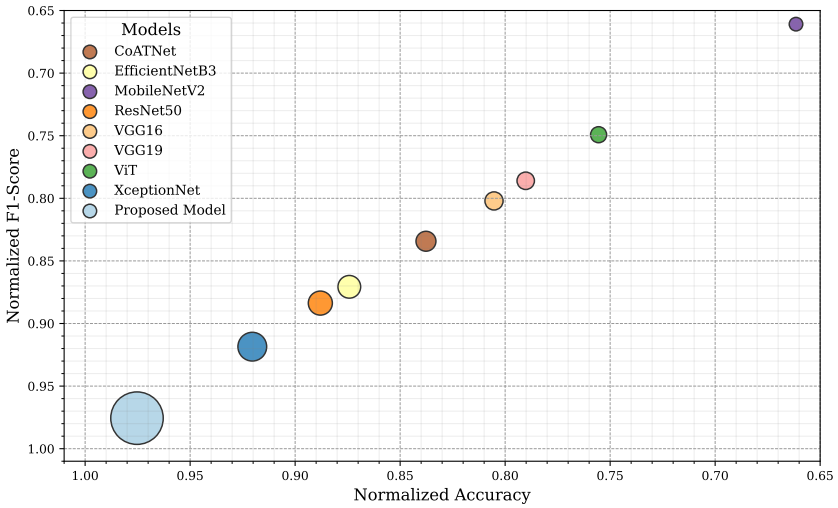

Figure 4: Accuracy vs. F1-score scatter plot for different model combinations for 128 batch size. Here, all of the models compete with each other to be the best-performing model. Best-performing model indicators are becoming larger in size as they are going towards the origin. The best-performing model is the one that is closest to the origin.

later prompts (P3 , P4) probe more targeted or assistive reasoning under additional guidance. As a result, P1 carries the highest weight (0.4) because it reflects the model's "raw" zero-shot capability without external scaffolding. P2 (0.3) evaluates slightly aided reasoning but still preserves open-ended model behavior. P3 (0.2) and P4 (0.1) contribute less to the final score because they increasingly rely on prompt cues and therefore represent less of the model's intrinsic reasoning ability. This descending weighting follows prior evaluation practice in LLM robustness studies, where unguided reasoning is considered the most informative indicator of general model performance.

The thresholds were chosen to produce the taxonomy of LLMs' performance. Models with (FinalScore > 0.80) consistently demonstrate stable predictions across all prompt levels with minimal sensitivity to wording changes, which aligns with our notion of a *Human-Like Reasoner*. Al-

Table 4: Performance of all DL architecture on stomach infection test dataset (5-Fold Evaluation) using Test Accuracy(%), Test Loss, F1-Score(%), Precision(%) Sensitivity(%), Specificity (%), Kappa(%)

Model	Test Accuracy (%)	F1-Score (%)	Precision (%)	Sensitivity (%)	Specificity (%)	Kappa (%)
CoATNet	83.77 ± 0.46	83.43 ± 0.51	83.78 ± 0.59	83.49 ± 0.52	82.30 ± 2.47	81.27 ± 0.60
EfficientNetB3	87.42 ± 0.21	87.07 ± 0.28	87.26 ± 0.31	87.07 ± 0.28	90.53 ± 2.33	85.37 ± 0.31
MobileNetV2	66.15 ± 1.00	66.09 ± 1.27	67.69 ± 0.98	66.16 ± 1.15	63.79 ± 7.14	61.47 ± 1.40
ResNet50	88.80 ± 1.71	88.37 ± 1.92	89.41 ± 1.19	88.59 ± 1.67	92.30 ± 5.26	87.11 ± 1.84
VGG16	80.53 ± 0.53	80.21 ± 0.62	80.56 ± 0.75	80.27 ± 0.65	81.75 ± 3.32	77.63 ± 0.74
VGG19	79.02 ± 1.11	78.60 ± 1.21	79.01 ± 1.28	78.63 ± 1.21	78.69 ± 3.40	75.76 ± 1.37
VIT	75.55 ± 2.00	74.92 ± 2.23	75.76 ± 1.57	75.18 ± 2.02	66.92 ± 11.66	71.89 ± 2.21
XceptionNet	92.04 ± 0.78	91.85 ± 0.82	92.09 ± 0.70	91.86 ± 0.81	92.78 ± 4.11	90.81 ± 0.91
MobileCoAtNet (Proposed)	97.53 ± 3.81	97.56 ± 3.81	97.62 ± 3.74	97.54 ± 3.82	97.52 ± 3.81	97.24 ± 4.31

Table 5: Performance evaluation of the MobileCoAtNet model with 5-fold cross-validation for eight different classes of stomach disease.

Network	Class	Fold	Test Accuracy (%)	F1 Score (%)	Sensitivity (%)	Precision (%)	Specificity (%)	Kappa (%)
Proposed Model	8 (Dyed lifted polyps, Dyed resection margins, Esophagitis, Normal cecum, Normal pylorus, Normal z line, Polyps, Ulcerative colitis)	Fold 1	99.15	99.29	99.27	99.34	99.03	99.19
		Fold 2	99.57	99.43	99.43	99.43	99.71	99.35
		Fold 3	99.43	99.58	99.56	99.60	99.30	99.51
		Fold 4	99.57	99.57	99.56	99.60	99.58	99.51
		Fold 5	89.91	89.94	89.90	90.14	89.92	88.62
		Average	97.53 ± 3.81	97.56 ± 3.81	97.54 ± 3.82	97.62 ± 3.74	97.52 ± 3.81	97.24 ± 4.31

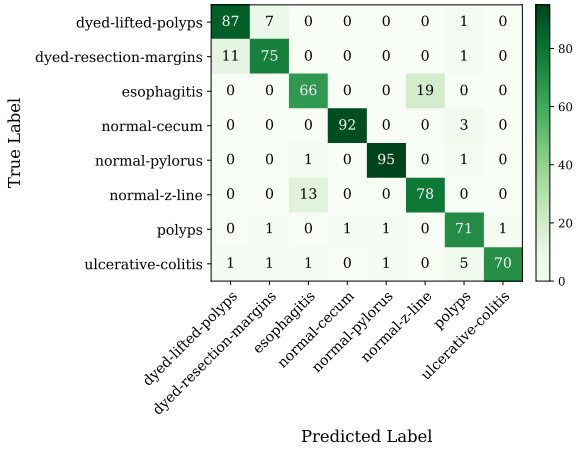

Figure 5: Confusion matrix for the proposed MobileCoAtNet model for the multi-class classification task.

though they show strong consistency, these models still require human supervision before being applied to sensitive or high-stakes tasks, as even small errors in such contexts can lead to real-world consequences. Scores between ($0.50 \leq$ FinalScore ≤ 0.80) indicate partial stability—these models perform well under some prompts but degrade under paraphrasing or adversarial phrasing, matching the characteristics of an *Adaptive Reasoner*. These models are generally more transferable and generalizable, but they are not ready for direct deployment in specialized domains. With domain adaptation or fine-tuning, however, they can become reliable for specific downstream tasks. Models with (FinalScore < 0.50) exhibit high prompt sensitivity, inconsistent reasoning chains, or frequent label flips, which we classify as *Failed / Unreliable Reasoner*. These models are not suitable for real-world use in their current state. To make them effective, they require structured retraining, improved instruction data, or carefully curated datasets targeted toward the intended downstream applications.

6 Results and Findings

In our experiment, we used two types of models to complete our framework- one inspired from CNN and the other by LLM. Initialy we select a list of models and found the best performing one after evaluating on task-specific benchmark data sets.

6.1 Performance Evaluation for DL Models

DL Model Selection

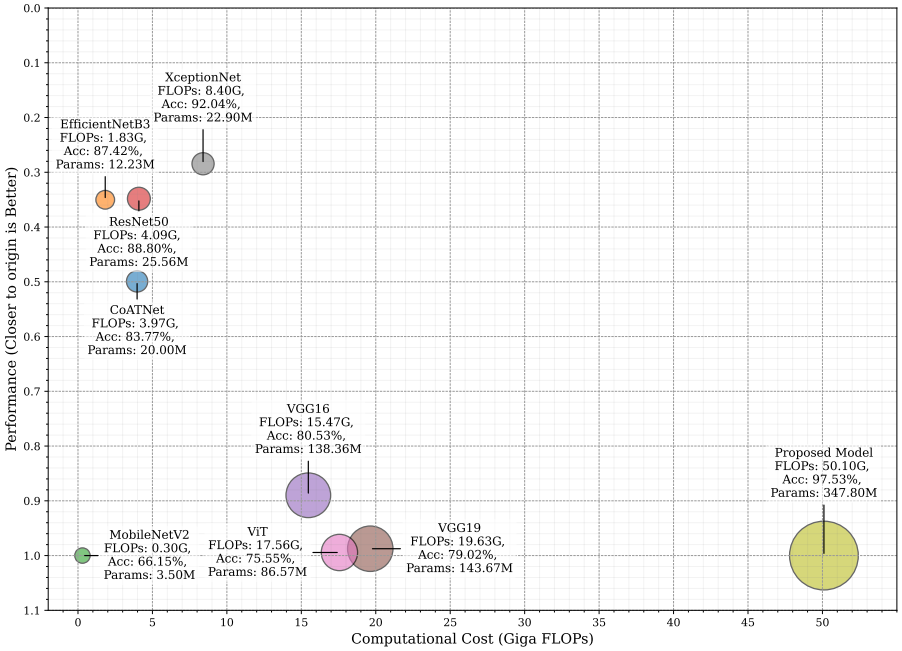

Figure 6: Model performance comparison based on accuracy (%) versus FLOPs (GigaFLOPs). The proposed MobileCoAtNet model achieves the highest accuracy with moderate computational demands, demonstrating its superiority in efficiency and effectiveness.

Table 6: Ablation study on CRS_{prompt} scores across different weight combinations to select the best combination.

Weight setting (w_1,w_2,w_3)	**Gemini-1.5**	**Gemini-1.5-8B**	**Gemini-1.5-Pro**	**Gemini-2.0**	**GPT-3.5**	**GPT-4.1**	**GPT-4.1-mini**	**GPT-4.1-nano**
$(0.2, 0.3, 0.5)$	0.1864	0.1990	0.1724	0.1960	0.1957	0.2436	0.2476	0.1946
$(0.2, 0.4, 0.4)$	0.1754	0.1874	0.1624	0.1844	0.1837	0.2287	0.2331	0.1835
$(0.2, 0.5, 0.3)$	0.1645	0.1758	0.1524	0.1727	0.1717	0.2138	0.2187	0.1723
$(0.3, 0.2, 0.5)$	0.2104	0.2242	0.1954	0.2218	0.2176	0.2758	0.2778	0.2191
$(0.3, 0.3, 0.4)$	0.1995	0.2126	0.1854	0.2101	0.2056	0.2609	0.2634	0.2080
$(0.3, 0.4, 0.3)$	0.1885	0.2010	0.1754	0.1985	0.1936	0.2460	0.2489	0.1969
$(0.3, 0.5, 0.2)$	0.1776	0.1894	0.1654	0.1869	0.1816	0.2311	0.2344	0.1858
$(0.4, 0.2, 0.4)$	0.2235	0.2378	0.2084	0.2359	0.2275	0.2930	0.2936	0.2326
$(0.4, 0.3, 0.3)$	0.2126	0.2262	0.1984	0.2243	0.2155	0.2782	0.2791	0.2214
$(0.4, 0.4, 0.2)$	0.2016	0.2147	0.1884	0.2127	0.2036	0.2633	0.2647	0.2103
$\mathbf{(0.5, 0.2, 0.3)}$	**0.2366**	**0.2514**	**0.2214**	**0.2501**	**0.2374**	**0.3103**	**0.3094**	**0.2460**
$(0.5, 0.3, 0.2)$	0.2257	0.2399	0.2114	0.2384	0.2255	0.2954	0.2949	0.2349

At first, we selected twenty-five DL models from nine different architecture families based on parameter size. We selected a subset of 500 data samples from our dataset (Pogorelov et al., 2017). We used a set of evaluation metrics: test accuracy, F1 score, precision, sensitivity, and Cohen's kappa. We evaluated the models on the selected data sample using a zero-shot mechanism. We sorted the models based on F1-score and selected the best-performing eight models for further experimentation.

B. Best Performing DL Model Selection

We performed five-fold cross-validation on the selected eight models from zero-shot based model selection along with our proposed MobileCoAtNet to find the best performing model refer to Table 4.

The proposed MobileCoAtNet model along with eight selected models, was fine-tuned and evaluated on eight classes: dyed lifted polyps, dyed resection margins, esophagitis, normal cecum, normal pylorus, normal Z-line, Polyps, and ulcerative colitis. As summarised in Table 5, the model demonstrates consistently high performance across the first four folds, achieving test accuracies between 99.15% and 99.57%, with corresponding F1 scores ranging from 99.29% to 99.58% and low test losses between 0.0209 and 0.0475. The confusion matrix in Figure 5 shows a strong diagonal dominance, indicates most samples are classified correctly and the proposed model can separate the gastrointestinal classes well. In

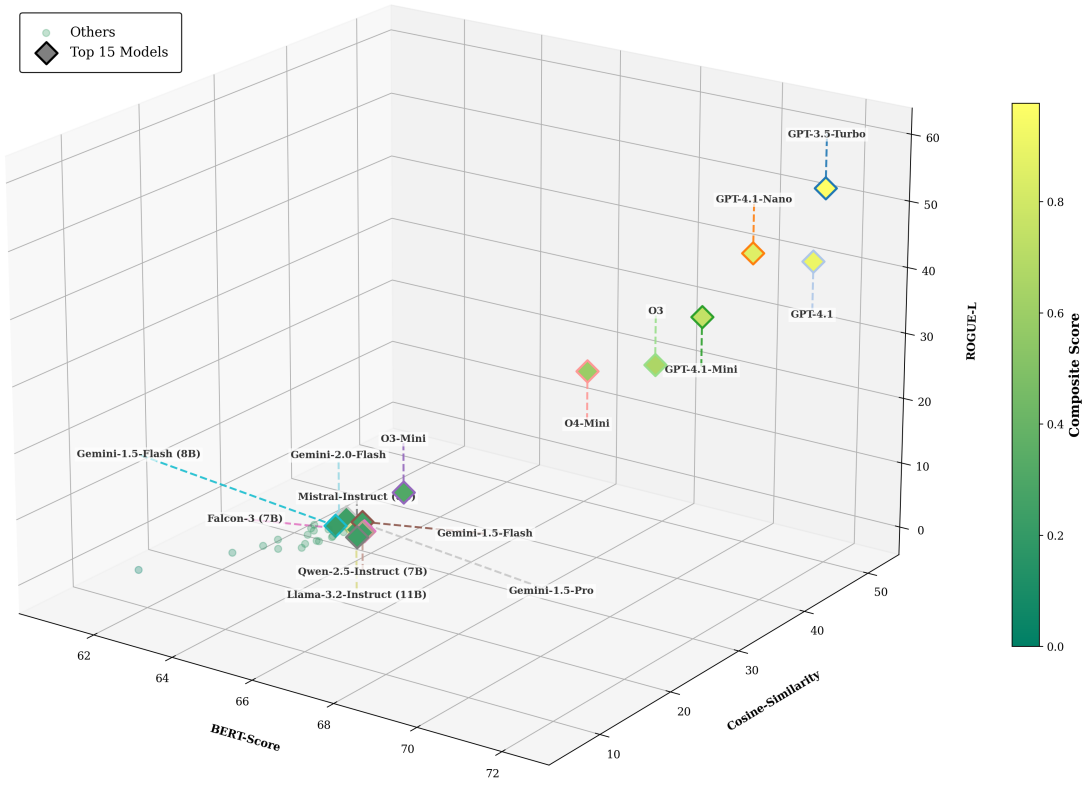

Figure 7: Top 15 LLM selection using the composite score, which is calculated using four $\text{CRS}_{\text{prompt}}$ scores.

contrast, performance in Fold five is comparatively lower, with a test accuracy of 89.91%, and an F1 score of 89.94%. Our Proposed model achieved the highest score with an average test accuracy of $97.53 \pm 3.81\%$ and mean F1 score $97.56 \pm 3.81\%$ across five different folds.

After evaluating other 8 models XceptionNet was found as second best performer with test accuracy of (92.04% $\pm$ 0.78) and F1 score of (91.85% $\pm$ 0.82). The performance comparison of nine selected models including our proposed one (MobileCoAtNet) shows that MobileCoAtNet achieved the strongest performance with a large performance gap even with the second best performing model, which is evident by Figure 4 (Accuracy vs F1 Score).

C. Quantitative Analysis

The comparison of accuracy and computational cost is shown in Figure 6. The proposed MobileCoAtNet achieves the highest accuracy at 97.53% and operates at 50.10 GigaFLOPs with 347.80M parameters, which is expected for a model optimized for maximum performance. Among the efficient models, MobileNetV2 and EfficientNetB3 stand out. MobileNetV2 has the lowest computational cost at 0.30 GigaFLOPs and reaches 66.15% accuracy. EfficientNetB3 offers a balanced result with 87.42% accuracy at 1.83 GigaFLOPs. XceptionNet also presents a strong trade-off, achieving 92.04% accuracy with 8.40 GigaFLOPs. VGG16 (15.47 GigaFLOPs, 80.53% accuracy) and VGG19 (19.63 GigaFLOPs, 79.02% accuracy) provide moderate performance but at a higher computational cost.

6.2 Performance Evaluation for LLM-based Multi-step Reasoning

6.2.1 LLM selection

At first 32 models were selected from 7 different families based on parameter size. The selected models were first evaluated on Benchmark-1 (GastroLLM-Bench) using zero-shot prompting. Their reasoning performance was measured using three metrics - BERTScore, Cosine Similarity, and ROUGE-L. Based on these results, 15 models were chosen for further experiments. At this stage, GPT-4.1, GPT-3.5-Turbo, GPT-4.1-Nano, GPT-4.1-Mini, O3, O4-Mini, O3-Mini, and Gemini-1.5-Flash showed consistently strong performance across all disease classes.

To identify the best-performing models, we created a composite score by normalizing BERTScore, cosine similarity, and ROUGE-L, and then aver-

Table 7: Final leaderboard for DL^{3}M-based clinical reasoning generation.

Rank	Model	CRS (P1)	CRS (P2)	CRS (P3)	CRS (P4)	Final Score	Category
1	**GPT 4.1**	0.537	0.529	0.519	0.523	**0.530**	**Adaptive**
2	**GPT 4.1 Mini**	0.531	0.527	0.485	0.481	**0.515**	**Adaptive**
3	**Gemini 1.5 Flash 8b**	0.462	0.474	0.477	0.487	**0.471**	**Unreliable**
4	**GPT 3.5 turbo**	0.464	0.459	0.483	0.496	**0.470**	**Unreliable**
5	**GPT 4.1 Nano**	0.440	0.469	0.503	0.498	**0.467**	**Unreliable**
6	**Gemini 2.0 Flash**	0.454	0.472	0.482	0.454	**0.465**	**Unreliable**
7	**O3**	0.462	0.462	0.459	0.471	**0.462**	**Unreliable**
8	**Gemini 1.5 Pro**	0.445	0.447	0.497	0.480	**0.460**	**Unreliable**
9	**Gemini 1.5 Flash**	0.426	0.460	0.473	0.482	**0.451**	**Unreliable**
10	**O4-Mini**	0.445	0.449	0.443	0.276	**0.429**	**Unreliable**
11	**O3-Mini**	0.234	0.234	0.234	0.234	**0.234**	**Unreliable**

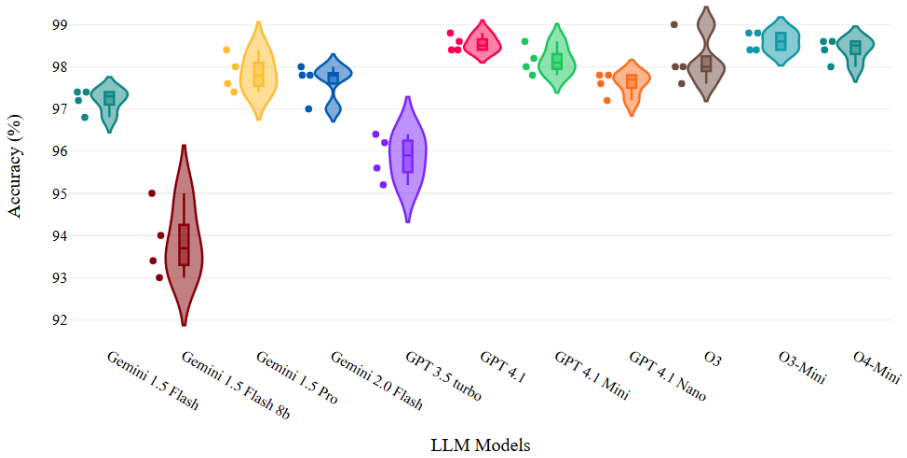

(a) Prompt sensitivity in LLM for four different directive levels for the multiple-choice task.

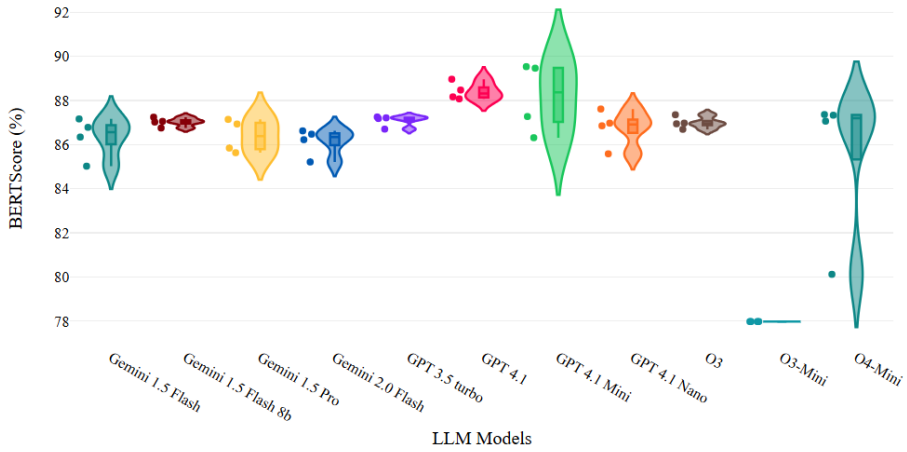

(b) Prompt sensitivity in LLM for four different directive levels for the multi-step reasoning task.

Figure 8: Violin plot for prompt sensitivity evaluation in (a) multiple-choice and (b) reasoning tasks.

aging the normalized values. This provided a balanced measure of semantic alignment, contextual consistency, and overall reasoning quality. The results reveal a clear pattern: among the top fifteen models, eleven were proprietary, and only four were open-source. This indicates that commercial models currently hold a noticeable advantage in medical reasoning tasks. Models with more than seven billion parameters also tended to perform better. This experiment suggests that larger parameter counts still play an important role in capturing clinical nuance and producing stable reasoning. The strongest results were observed across seven major model families. These included four models

Table 8: Zero-shot-based initial LLM evaluation to select the best models for the clinical reasoning experiment.

Model	BERT-Score	Cosine-Similarity	ROUGE-L
Deep Seek R1 (8B) (DeepSeek-AI, 2025)	65.28	13.57	8.09
Deep Seek R1 (14B) (DeepSeek-AI, 2025)	65.79	13.16	10.14
Deep Seek R1 (32B) (DeepSeek-AI, 2025)	65.51	13.99	10.81
Falcon (7B) (Penedo et al., 2023)	65.64	12.11	10.11
Falcon-3 (7B) (Penedo et al., 2023)	66.31	16.44	10.64
Mistral-Instruct (8B) (Jiang et al., 2023)	66.40	14.99	10.67
Mistral-Instruct (7B) (Jiang et al., 2023)	66.01	13.72	10.78
Llama-3.1-Instruct (8B) (AI@Meta, 2024)	65.70	15.51	9.41
Llama-3.2-Instruct (1B) (AI@Meta, 2024)	64.05	10.83	6.94
Llama-3.2-Instruct (3B) (AI@Meta, 2024)	64.90	12.44	7.97
Llama-3.2-Instruct (11B) (AI@Meta, 2024)	66.00	17.06	10.01
Qwen-2.5-Instruct (1.5B) (Bai et al., 2024)	65.28	15.58	7.99
Qwen-2.5-Instruct (7B) (Bai et al., 2024)	66.41	15.66	11.02
Qwen-3 (4B) (Team, 2025)	64.55	12.29	7.95
Qwen-3 (8B) (Team, 2025)	65.16	15.02	9.03
Qwen-3 (14B) (Team, 2025)	65.67	17.13	9.04
Gemma-2 (2B) (Team, 2024b)	62.53	6.33	4.48
Gemma-2 (9B) (Team, 2024b)	64.68	13.59	8.35
Gemini-1.5-Flash (8B) (Reid et al., 2024)	65.89	14.84	11.66
Gemini-1.5-Flash (Reid et al., 2024)	66.24	16.59	11.83
Gemini-1.5-Pro (Reid et al., 2024)	65.69	17.39	11.19
Gemini-2.0-Flash-Lite (Team, 2024a)	65.38	14.32	10.77
Gemini-2.0-Flash (Team, 2024a)	65.56	17.13	10.45
Gemini-2.5-Flash (DeepMind, 2025)	65.38	16.66	9.26
Gemini-2.5-Pro (DeepMind, 2025)	64.94	17.09	9.00
O3 (Brown et al., 2020)	70.20	35.02	31.37
O3-Mini (Brown et al., 2020)	66.42	21.27	13.91
O4-Mini (Brown et al., 2020)	68.95	32.70	29.83
GPT-3.5-Turbo (OpenAI, 2023)	71.59	51.70	51.55
GPT-4.1-Nano (OpenAI, 2023)	71.02	44.35	44.54
GPT-4.1-Mini (OpenAI, 2023)	70.48	40.19	36.29
GPT-4.1 (OpenAI, 2023)	72.26	45.61	44.41

from OpenAI's GPT series, three from OpenAI's reasoning-oriented models, four from the Gemini family, and one model each from the Qwen, LLaMA, Mistral, and Falcon families. This range shows that high performance is not restricted to a single architecture, but it also highlights that only a small portion of the broader LLM ecosystem is capable of generating consistent, medically grounded explanations.

6.2.2 Multiple Choice Task

In the classification stage, the LLMs were evaluated based on their responses to multiple-choice questions. The results were assessed using Accuracy, F1 Score, and Cohen's Kappa metrics (Table 9 and 10).

(a) Small Model (less than 10 billion parameters): Among the small models, Gemini-1.5-Flash, Gemini-2.0-Flash, GPT-4.1-Mini, GPT-4.1-Nano, and Gemini-1.5-Flash (8B) performed strongly, with accuracy, F1 Score, and Cohen's kappa all above 85%. For an LLM, achieving high scores across these metrics indicates more than correct classification—it reflects better contextual understanding, stronger semantic alignment with clinical descriptions, and more consistent reasoning across samples. In contrast, Mistral-8B and Falcon-3 7B Base stayed below 50% on all three metrics, suggesting weaker domain grounding, frequent confusion between clinically similar classes, and limited agreement with expected reasoning patterns. Since both are open-source, they still have room for improvement through targeted fine-tuning. Performance on the Polyp class showed greater variation. Gemini-1.5-Flash reached roughly 91% accuracy with an F1 score of 80% and a Cohen's kappa of 84%, indicating strong sensitivity to the features associated with polyp-related cases. Gemini-1.5-Flash (8B) achieved around 80% accuracy but dropped to an F1 score of 57% and a kappa of 53%, suggesting difficulty with borderline cases and reduced stability when distinguishing this class from similar conditions. Even so, both models performed well across the remaining disease classes, implying that these weaknesses are limited to specific categories. All five proprietary models re-

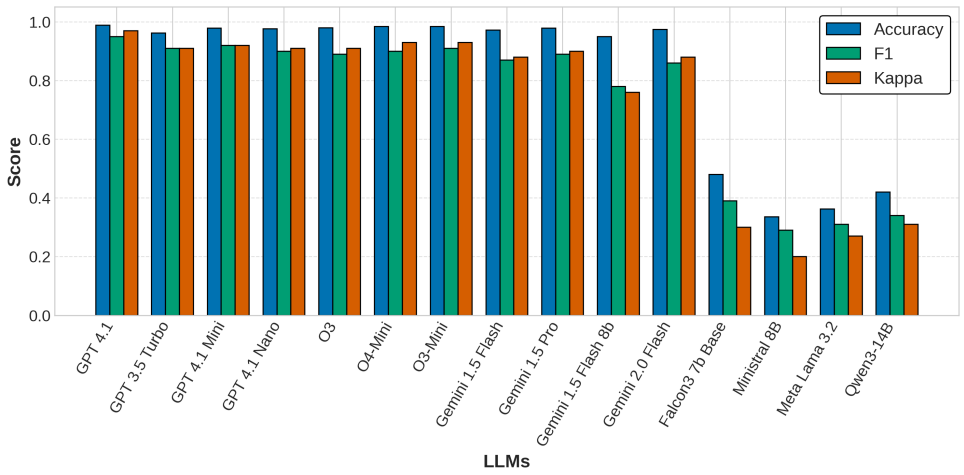

(a) Performance evaluation on the multiple-choice task using prompt-1.

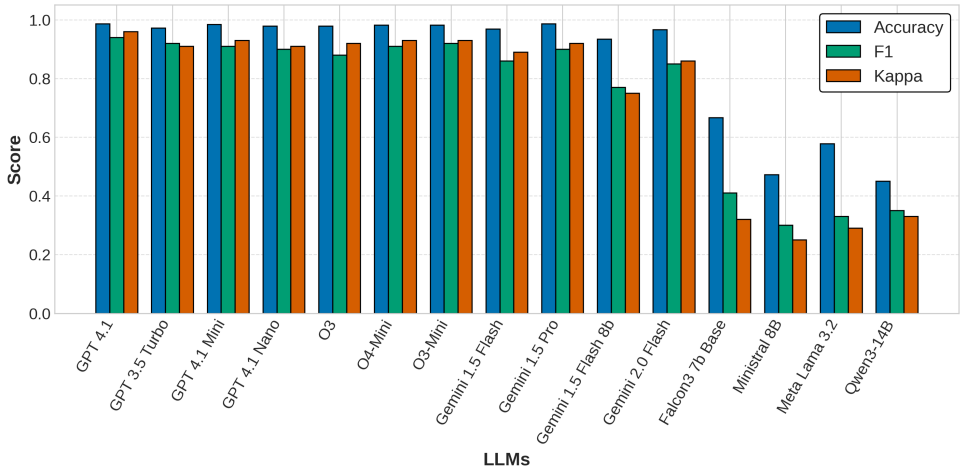

(b) Performance evaluation on the multiple-choice task using prompt-2.

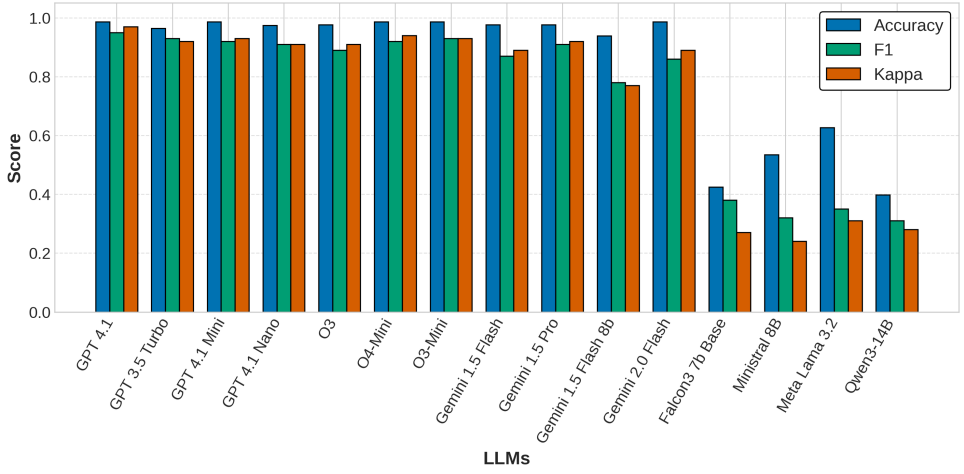

(c) Performance evaluation on the multiple-choice task using prompt-3.

mained stable across different prompts, showing deeper domain understanding, stronger semantic robustness, and less dependence on prompt wording. Among the weaker models, Mistral-8B produced its best results under Prompt 4, while Falcon-3 7B Base performed better under Prompt 2 but declined under Prompt 4, highlighting their sensitivity to prompt formulation and their limited ability to gen-

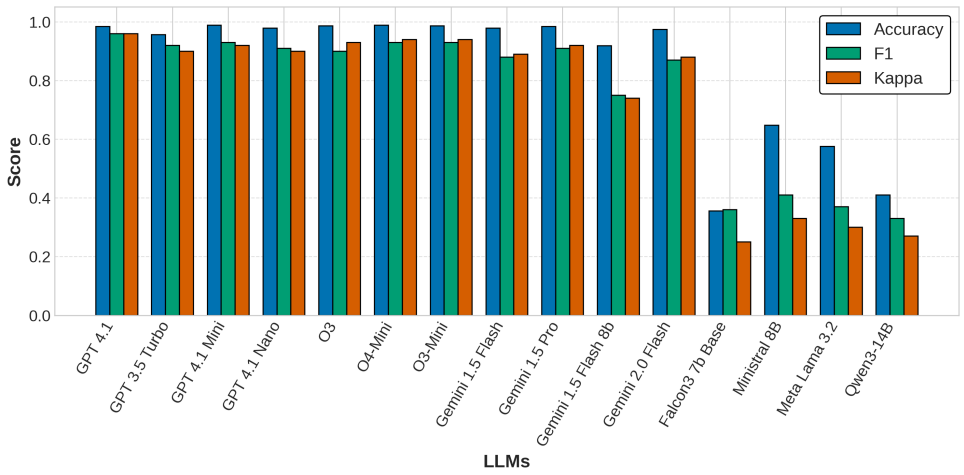

(d) Performance evaluation on the multiple-choice task using prompt-4.

Figure 9: Performance evaluation of fifteen best LLMs with four different levels of prompts for the multiple-choice task.

eralize reasoning across varying prompting conditions.

(b) Mid-Size Models (Parameter size $> 10B$ and $< 50B$): Among the four mid-size models, GPT-4.1-Mini and GPT-3.5-Turbo performed strongly, scoring above 85% on all evaluation metrics. Their higher scores suggest better contextual understanding and more stable alignment with the clinical reasoning patterns expected in this task. In contrast, LLaMA-3.2 (11B) and Qwen-3 (14B) showed weaker performance, with all metrics falling below 60%. This indicates limitations in their ability to capture medical nuance, maintain semantic consistency, or generalize across different reasoning prompts. Both lower-performing models are open-source, making them strong candidates for domain-specific fine-tuning to address these gaps and improve their reasoning quality.

(c) Large Models (Parameter size $> 50B$): All four large models - O3-Mini, Gemini-1.5-Pro, GPT-4.1, and O3, performed strongly, with scores above 90% across all evaluation metrics. Although their performance dipped slightly for the Esophagitis, Polyp, and Ulcerative Colitis classes, they achieved perfect scores for the Healthy and Removal of Lesions classes, showing strong alignment with cases that present clearer visual and clinical cues. All four models remained stable across most prompt variations, though a small decline appeared under Prompt 3, suggesting that certain forms of reasoning still introduce mild instability even in high-capacity models.

When comparing all 15 models, the top five performers were O3-Mini, with 99% accuracy, an F1 score of 94%, and a Cohen's kappa of 96%; Gemini-1.5-Pro, with 98% accuracy, an F1 of 95%, and a kappa of 95%; O4-Mini, with 98% accuracy, an F1 of 92%, and a kappa of 95%; GPT-4.1, with 99% accuracy, an F1 of 90%, and a kappa of 97%; and O3, with 98% accuracy, an F1 of 91%, and a kappa of 96%. Four of these five models exceed 200 billion parameters, reinforcing the value of large-scale architectures for clinically grounded reasoning. At this stage of the analysis, only models scoring above 80% on all three metrics were retained for the reasoning-label evaluation. Four models—Mistral-8B, Falcon-3 7B Base, Qwen-3 14B, and Llama-3.2 11B—did not meet this threshold. Notably, all four are open-source models, highlighting a clear performance gap between proprietary and open-source systems in medical reasoning tasks, likely driven by differences in training data quality, model scale, and domain exposure.

6.2.3 Reasoning Genaration Task

Three metrics were used to evaluate the reasoning outputs: BERTScore, cosine similarity, and ROUGE-L. In the BERTScore analysis, 10 of the 11 models performed well. GPT-4.1 and GPT-4.1 Mini led with scores of 88%, followed closely by GPT-3.5 Turbo, Gemini 1.5 Flash 8B, O3, and GPT-4.1 Nano, each scoring 87%. Gemini 1.5 Pro, Gemini 1.5 Flash, and Gemini 2.0 Flash showed slightly lower but still strong scores of 86%, while O4-Mini reached 85%. The weakest performance came from O3-Mini, which achieved 78%.

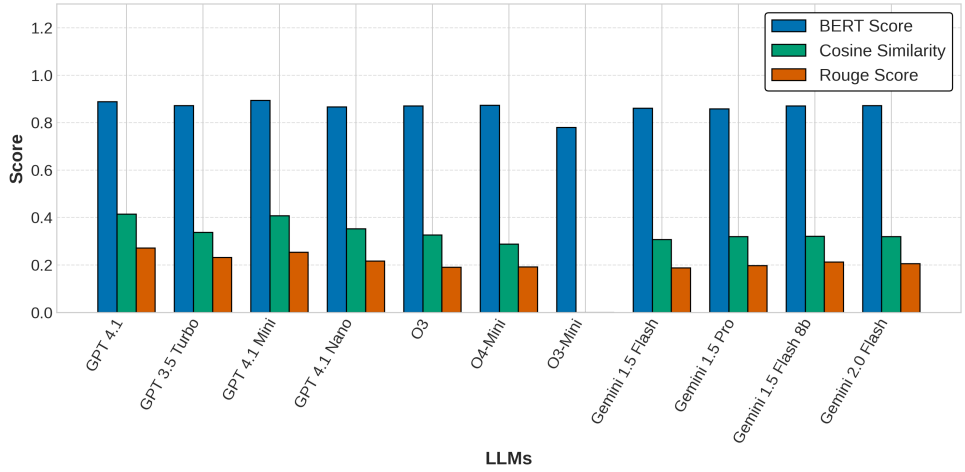

(a) Performance evaluation on the multiple-step reasoning task using prompt-1.

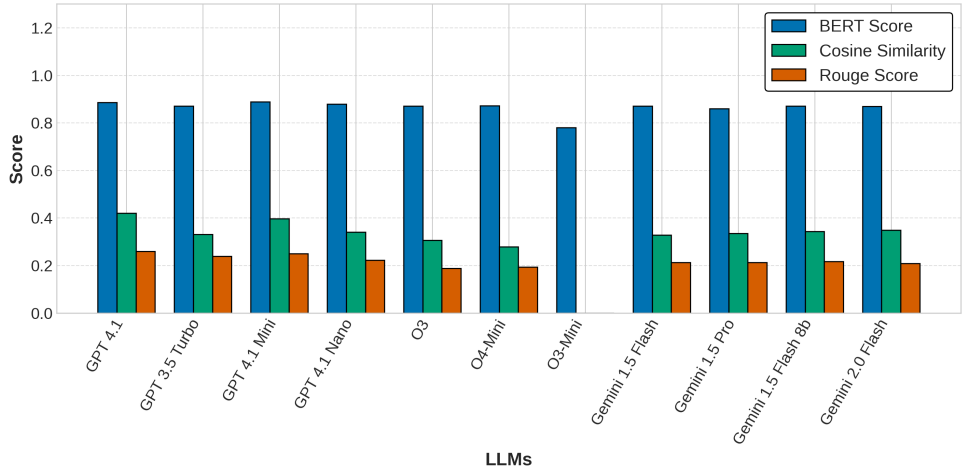

(b) Performance evaluation on the multiple-step reasoning task using prompt-2.

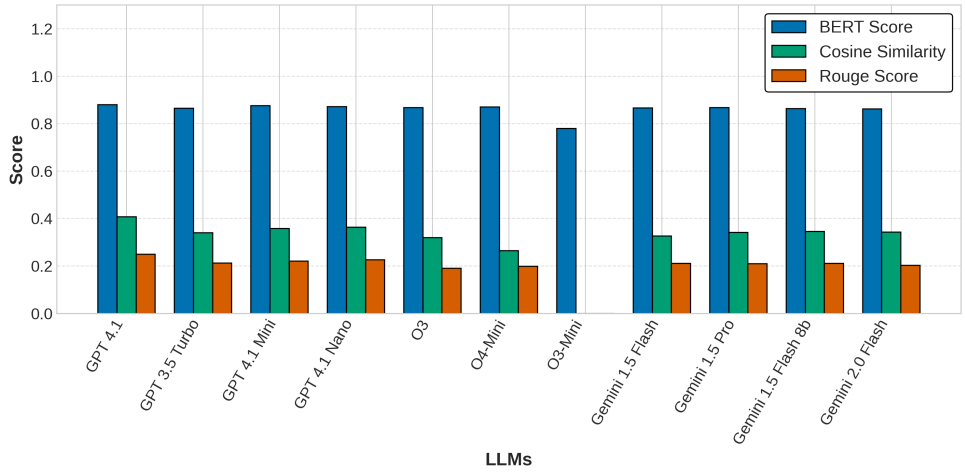

(c) Performance evaluation on the multiple-step reasoning task using prompt-3.

For cosine similarity, GPT-4.1, GPT-4.1 Mini, and GPT-4.1 Nano again ranked highest with scores of 42%, 39%, and 35%. Gemini 1.5 Flash 8B, GPT-3.5 Turbo, and Gemini 1.5 Pro each obtained 0.34. Gemini 2.0 Flash and O3 scored 33%, followed by Gemini 1.5 Flash with 32%. O4-Mini dropped to 23%, and O3-Mini recorded the lowest value of 0.00. The ROUGE-L results followed a similar pattern. GPT-4.1 scored highest at 25.5%, with GPT-4.1 Mini next at 23.6%. GPT-3.5 Turbo reached 21.9%, while Gemini 1.5 Flash 8B and GPT-4.1 Nano scored 0.210 and 0.203. Gemini

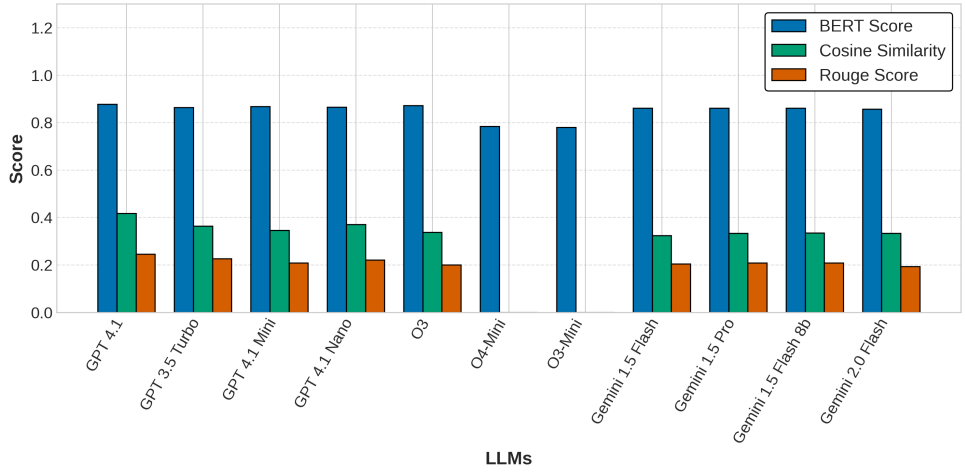

(d) Performance evaluation on the multiple-step reasoning task using prompt-4.

Figure 10: Performance evaluation of fifteen best LLMs with four different levels of prompts for the multiple-step reasoning task.

2.0 Flash and Gemini 1.5 Pro produced comparable values of 20% and 19.8%, and Gemini 1.5 Flash and O3 scored 19.6% and 19.1%. O4-Mini dropped to 15.9%, while O3-Mini again showed no measurable performance with 0.000.

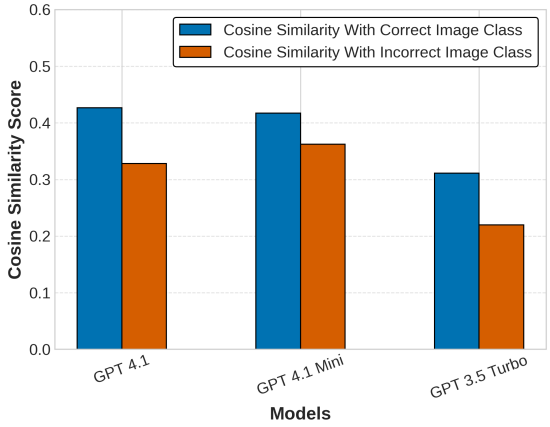

Figure 11: Performance comparison for multi-step reasoning generation of the best-performing LLMs in two different settings, when the image is predicted correctly and when the image is mispredicted from the proposed MobileCoAtNet (DL model).

Overall, GPT-4.1 and GPT-4.1 Mini consistently ranked at the top across all three metrics. Although these LLMs performed the highest for correct image labels (when the DL model predicts an image class correctly), they fall short for incorrect image classes refer to Figure 11. Again, the strongest models show noticeable gaps in semantic alignment, stability, and contextual consistency, indicating that none of them can yet be trusted to produce reasoning outputs without human oversight.

6.2.4 Analysis of the best performance LLM with human expertise

As the results in Table 7 show, no model achieved the 'Human-Like' status. The top models, **GPT 4.1** (53%) and **GPT 4.1 Mini** (51.5%), fall into the 'Adaptive' category, indicating they provide competent reasoning, especially on general prompts. The remaining models, including the **Gemini series** and **GPT 3.5 turbo**, are now categorized as 'Unreliable' under this strict threshold, as their ability to reason with minimal context falls below the 50% cutoff.

7 Discussion

In our study we show that combining deep-learning–based disease classification with LLM-driven reasoning helps narrow the gap between image recognition and clinical explanation, but it also exposes several limitations. For RQ_1, our results show that the quality of classification directly shapes the quality of reasoning. Because LLMs cannot interpret images on their own and rely entirely on the predicted class label, a correct prediction leads to meaningful clinical reasoning, while an incorrect prediction immediately results in flawed explanations. This makes upstream classification accuracy essential. For RQ_2, we find that LLMs are capable of producing useful, multi-step clinical reasoning when the DL model's prediction is correct. They can describe causes, symptoms, treatment options, dietary suggestions, and

follow-up care. However, their performance varies across model sizes: larger models tend to be more consistent and detailed, while smaller models depend heavily on prompt wording and often miss important medical details. For RQ_3, our findings indicate that no current LLM produces reasoning that matches expert-level judgment. Although future models may come closer to expert reasoning, they would still require supervision before being used in sensitive medical environments. More adaptive models will need domain adaptation or fine-tuning to be reliable, while less consistent models will require substantial retraining with structured datasets before they can be trusted. Finally, the study demonstrates that while the **DL^{3}M** pipeline improves interpretability and clinical alignment compared to using either model alone, its reliability still depends on accurate classification, selecting appropriate LLMs, careful prompt design, and continuous human oversight - especially in medical settings where errors can have serious consequences.

8 Conclusion

From our experiment we present a complete view, how DL–based disease classification and LLMs can work together to support clinical reasoning in gastrointestinal diagnosis. The results show that combining a reliable classifier with an LLM helps bridge the gap between what is visible in an endoscopic image and the type of explanation a clinician expects. When the classifier's prediction is correct, most LLMs can generate structured and medically meaningful reasoning, including causes, symptoms, treatment options, lifestyle guidance, and follow-up care. However, the findings also make it clear that the entire pipeline depends heavily on upstream accuracy - any classification error leads directly to flawed reasoning because LLMs cannot interpret images on their own and rely entirely on the predicted label.

Our proposed method integrates DL with LLMs to bring gastrointestinal diagnosis closer to transparent, interpretable, and multi-step reasoning systems that resemble expert thinking. The pipeline illustrates how automated disease detection can be extended into clinically meaningful explanations, pointing toward decision-support tools that better align with real-world clinical needs. This work lays the foundation for developing reasoning models that are not only more informative but also more consistent with expert interpretive patterns. This creates a new direction for future experiments and contribute more effectively to clinical decision-making.

9 Limitations and Future Work

In our experiment some models, especially the larger ones produce more stable and clinically aligned explanations but none of them consistently achieve expert-level reasoning. Smaller models often miss contextual details, struggle with medical nuance, and show greater sensitivity to prompt design. Even the strongest models display variation across disease classes and prompt types, indicating that they still fall short of the consistency and reliability needed for real clinical use.

Future research should aim to make LLM-based reasoning more dependable and medically grounded. One direction is to strengthen the **DL^{3}M** pipeline by improving disease-prediction accuracy, incorporating uncertainty estimation, and enabling LLMs to handle ambiguous or borderline cases more effectively. Another important direction is the development of domain-adapted LLMs trained specifically on gastrointestinal data, allowing their reasoning to reflect expert-level knowledge rather than broad, general medical patterns. For models that behave inconsistently, structured fine-tuning and reinforcement learning with clinician-verified feedback may help improve stability and reliability. A more robust evaluation setup is also needed, one that goes beyond textual similarity to measure factual correctness, clinical validity, and risk awareness. Finally, future systems should work toward real-time clinical decision support, where the LLM can interact with clinicians, ask clarifying questions, and justify its recommendations in a transparent manner. These developments can help shift current adaptive but unreliable models into trustworthy tools for sensitive medical tasks such as stomach-infection assessment, polyp management, and broader GI disease reasoning.

References

Reem Agbareia, Mahmud Omar, Shelly Soffer, Benjamin S Glicksberg, Girish N Nadkarni, and Eyal Klang. 2025. Visual-textual integration in llms for medical diagnosis: A preliminary quantitative analysis. *Computational and Structural Biotechnology Journal*, 27:184–189.

Md. Faysal Ahamed, Md. Nahiduzzaman, Md. Rabiul Islam, Mansura Naznine, Mohamed Arselene

Ayari, Amith Khandakar, and Julfikar Haider. 2024a. Detection of various gastrointestinal tract diseases through a deep learning method with ensemble elm and explainable ai. *Expert Systems with Applications*, 256:124908.

Md Faysal Ahamed, Md Nahiduzzaman, Md Rabiul Islam, Mansura Naznine, Mohamed Arselene Ayari, Amith Khandakar, and Julfikar Haider. 2024b. Detection of various gastrointestinal tract diseases through a deep learning method with ensemble elm and explainable ai. *Expert Systems with Applications*, 256:124908.

Md Faysal Ahamed, Md Nahiduzzaman, Md Rabiul Islam, Mansura Naznine, Mohamed Arselene Ayari, Amith Khandakar, and Julfikar Haider. 2024c. Detection of various gastrointestinal tract diseases through a deep learning method with ensemble elm and explainable ai. *Expert Systems with Applications*, 256:124908.

Istiak Ahmad and Fahad Alqurashi. 2024. Early cancer detection using deep learning and medical imaging: A survey. *Critical Reviews in Oncology/Hematology*, 204:104528.

AI@Meta. 2024. Llama 3: Open and efficient foundation language models. *ArXiv*.

Mousa Alhajlah, M Nouman Noor, Muhammad Nazir, Awais Mahmood, Imran Ashraf, and Tehmina Karamat. 2023. Gastrointestinal diseases classification using deep transfer learning and features optimization. *Comput. Mater. Contin*, 75(1):2227–2245.

Chunjiang Bai and 1 others. 2024. Qwen2 technical report. *ArXiv*.

Tom B Brown, Benjamin Mann, Nick Ryder, and 1 others. 2020. Language models are few-shot learners. In *Advances in Neural Information Processing Systems*, volume 33, pages 1877–1901.

François Chollet. 2017a. Xception: Deep learning with depthwise separable convolutions. In *2017 IEEE Conference on Computer Vision and Pattern Recognition (CVPR)*, pages 1800–1807.

François Chollet. 2017b. Xception: Deep learning with depthwise separable convolutions. In *IEEE Conference on Computer Vision and Pattern Recognition*, pages 1251–1258.

Xiaoyi Chong, Yelizhati Madeti, Jieyuan Cai, Wenfei Li, Lin Cong, Jialin Lu, Liyang Mo, Huizhen Liu, Siyi He, Chao Yu, and 1 others. 2024. Recent developments in immunotherapy for gastrointestinal tract cancers. *Journal of Hematology & Oncology*, 17(1):65.

Amit Das, Md Najib Hasan, Souvika Sarkar, Zheng Zhang, Fatemeh Jamshidi, Tathagata Bhattacharya, Nilanjana Raychawdhury, Dongji Feng, Vinija Jain, and Aman Chadha. 2025. Investigating hallucination in conversations for low resource languages. *arXiv preprint arXiv:2507.22720*.

Amit Das, Zheng Zhang, Najib Hasan, Souvika Sarkar, Fatemeh Jamshidi, Tathagata Bhattacharya, Mostafa Rahgouy, Nilanjana Raychawdhary, Dongji Feng, Vinija Jain, and 1 others. 2024. Investigating annotator bias in large language models for hate speech detection. *arXiv preprint arXiv:2406.11109*.

Google DeepMind. 2025. Gemini 2.5: Frontier multimodal reasoning models. *ArXiv*.

DeepSeek-AI. 2025. Deepseek-r1: Incentivizing reasoning capability in llms via reinforcement learning. *ArXiv*.

Ayşe Ayyüce Demirbaş, Hüseyin Üzen, and Hüseyin Fırat. 2024. Spatial-attention convmixer architecture for classification and detection of gastrointestinal diseases using the kvasir dataset. *Health Information Science and Systems*, 12(1):32.

Alexey Dosovitskiy, Lucas Beyer, Alexander Kolesnikov, Dirk Weissenborn, Xiaohua Zhai, Thomas Unterthiner, Mostafa Dehghani, Matthias Minderer, Georg Heigold, Sylvain Gelly, Jakob Uszkoreit, and Neil Houlsby. 2021a. An image is worth 16x16 words: Transformers for image recognition at scale. In *International Conference on Learning Representations*.

Alexey Dosovitskiy, Lucas Beyer, Alexander Kolesnikov, Dirk Weissenborn, Xiaohua Zhai, Thomas Unterthiner, Mostafa Dehghani, Matthias Minderer, Georg Heigold, and 1 others. 2021b. An image is worth 16x16 words: Transformers for image recognition at scale. In *International Conference on Learning Representations*.

Omar El Ogri, Jaouad EL-Mekkaoui, and Amal Hjouji. 2026. A computer-assisted medical diagnosis system for cancer diseases based on quaternion orthogonal rademacher-fourier moments and deep learning. *Biomedical Signal Processing and Control*, 112:108744.

Tahasin Ahmed Fahim, Fatema Binte Alam, and Md Azad Hossain. 2025. Brain tumor detection, classification and segmentation by deep learning models from mri images: Recent approaches, challenges and future directions. *Array*, 28:100571.

Rodrigo Fernandes, Alexandre Pessoa, José Nogueira, Anselmo Paiva, Ishak Paçal, Marta Salgado, and António Cunha. 2024. Evaluation of deep learning models in search by example using capsule endoscopy images. *Procedia Computer Science*, 239:2065–2073.

Mohsen Ghorbian, Mostafa Ghobaei-Arani, and Saied Ghorbian. 2025. Transforming breast cancer diagnosis and treatment with large language models: A comprehensive survey. *Methods*, 239:85–110.

Khanisyah Erza Gumilar, Manggala Pasca Wardhana, Muhammad Ilham Aldika Akbar, Agung Sunarko Putra, Dharma Putra Perjuangan Banjarnahor, Ryan Saktika Mulyana, Ita Fatati, Zih-Ying Yu, Yu-Cheng Hsu, Erry Gumilar Dachlan, Chien-Hsing

Lu, Li-Na Liao, and Ming Tan. 2025. Artificial intelligence-large language models (ai-llms) for reliable and accurate cardiotocography (ctg) interpretation in obstetric practice. *Computational and Structural Biotechnology Journal*, 27:1140–1147.

Md Najib Hasan, Mohammad Fakhruddin Babar, Souvika Sarkar, Monowar Hasan, and Santu Karmaker. 2025a. Pitfalls of evaluating language models with open benchmarks. *arXiv preprint arXiv:2507.00460*.

Md Najib Hasan, Md Ehashan Rabbi Pial, Sunanda Das, Nazmul Siddique, and Hui Wang. 2025b. Dia-vxnet: A framework for automated diabetic eye disease detection using transfer learning with feature fusion network. *Biomedical Signal Processing and Control*, 100:106907.

Najib Hasan, Sourav Basak Shuvo, Mahadi Hasan Ankon, SM Taslim Uddin Raju, and Nazmul Siddique. 2025c. Transfusionnet: Framework for cervical cancer detection using deep learning with multilevel fusion. *Results in Engineering*, page 107174.

Abdul Haseeb, Muhammad Attique Khan, Majed Alhaisoni, Ghadah Aldehim, Leila Jamel, Usman Tariq, Taerang Kim, and Jae-Hyuk Cha. 2023. A fusion of residual blocks and stack auto encoder features for stomach cancer classification. *Computers, Materials and Continua*, 77(3):3895–3920.

Maham Hayat, Kambiz Kadkhodayan, Muhammad K Hasan, Mustafa A Arain, Natalie Cosgrove, Deepanshu Jain, Peter V Draganov, and Dennis Yang. 2025. Utility of texture-color enhancement and red dichromatic imaging during endoscopic resection. *VideoGIE*.

Kaiming He, Xiangyu Zhang, Shaoqing Ren, and Jian Sun. 2016a. Deep residual learning for image recognition. In *2016 IEEE Conference on Computer Vision and Pattern Recognition (CVPR)*, pages 770–778.

Kaiming He, Xiangyu Zhang, Shaoqing Ren, and Jian Sun. 2016b. Deep residual learning for image recognition. In *IEEE Conference on Computer Vision and Pattern Recognition*, pages 770–778.

Kaiming He, Xiangyu Zhang, Shaoqing Ren, and Jian Sun. 2016c. Identity mappings in deep residual networks. In *European Conference on Computer Vision*, pages 630–645. Springer.

Qi He, Sophia Bano, Omer F Ahmad, Bo Yang, Xin Chen, Pietro Valdastri, Laurence B Lovat, Danail Stoyanov, and Siyang Zuo. 2020. Deep learning-based anatomical site classification for upper gastrointestinal endoscopy. *International journal of computer assisted radiology and surgery*, 15(7):1085–1094.

Andrew Howard, Mark Sandler, Grace Chu, Liang-Chieh Chen, Bo Chen, Mingxing Tan, Weijun Wang, Yukun Zhu, Ruoming Pang, Vijay Vasudevan, and Quoc Le. 2019. Searching for mobilenetv3. In *IEEE International Conference on Computer Vision*, pages 1314–1324.

Gao Huang, Zhuang Liu, Laurens Van Der Maaten, and Kilian Q Weinberger. 2017. Densely connected convolutional networks. In *IEEE Conference on Computer Vision and Pattern Recognition*, pages 4700–4708.

Albert Q. Jiang and 1 others. 2023. Mistral 7b. *ArXiv*.

Beauden John, Popoola Victor Femi, Osagwu Nnenna Anestina, Oyedeji Oyedotun, Alade Adetutu Sefinat Anthony, Alade Adebisi Mustapha, Farinu Hamzah, Clementina Nelly, and Chukwuemeka Chinonyelum Obiageli Ebeye. 2024. Advancements in endoscopic techniques for early detection and minimally invasive treatment of gastrointestinal cancers: A review of diagnostic accuracy, clinical outcomes, and technological innovations. *N/A*.

Yoshino Kaneyasu, Yuichi Mine, Yoshie Niitani, Tsuyoshi Taji, Saori Takeda, Ryohei Tokinaga, Hideo Shigeishi, Toshinobu Takemoto, Naoya Kakimoto, Takeshi Murayama, and Kouji Ohta. 2025. Analysis of multimodal large language models on visually-based questions in the japanese national examination for dental hygienists: A preliminary comparative study. *Journal of Dental Sciences*.

Anup Karan, Himanshu Negandhi, Suhaib Hussain, Tomas Zapata, Dilip Mairembam, Hilde De Graeve, James Buchan, and Sanjay Zodpey. 2021. Size, composition and distribution of health workforce in india: why, and where to invest? *Human resources for health*, 19(1):39.

Muhammad Attique Khan, Usama Shafiq, Ameer Hamza, Anwar M Mirza, Jamel Baili, Dina Abdulaziz AlHammadi, Hee-Chan Cho, and Byoungchol Chang. 2025. A novel network-level fused deep learning architecture with shallow neural network classifier for gastrointestinal cancer classification from wireless capsule endoscopy images. *BMC Medical Informatics and Decision Making*, 25(1):150.

Zahid Farooq Khan, Muhammad Ramzan, Mudassar Raza, Muhammad Attique Khan, Khalid Iqbal, Taerang Kim, and Jae-Hyuk Cha. 2024. Deep convolutional neural networks for accurate classification of gastrointestinal tract syndromes. *CMC-COMPUTERS MATERIALS & CONTINUA*, 78(1):1207–1225.

Christiane Kulinna-Cosentini, Jacqueline C Hodge, and Ahmed Ba-Ssalamah. 2024. The role of radiology in diagnosing gastrointestinal tract perforation. *Best Practice & Research Clinical Gastroenterology*, 70:101928.

Vimal Kumar, Priyam Srivastava, Ashay Dwivedi, Ishan Budhiraja, Debjani Ghosh, Vikas Goyal, and Ruchika Arora. 2024. Large-language-models (llm)-based ai chatbots: Architecture, in-depth analysis and their performance evaluation. In *Recent Trends in Image Processing and Pattern Recognition*, pages 237–249, Cham. Springer Nature Switzerland.

Yihao Li, Mostafa El Habib Daho, Pierre-Henri Conze, Rachid Zeghlache, Hugo Le Boité, Ramin Tadayoni, Béatrice Cochener, Mathieu Lamard, and Gwenolé Quellec. 2024. A review of deep learning-based information fusion techniques for multimodal medical image classification. *Computers in Biology and Medicine*, 177:108635.

Jiaxi Lin, Shiqi Zhu, Xin Gao, Xiaolin Liu, Chunfang Xu, Zhonghua Xu, and Jinzhou Zhu. 2024. Evaluation of super resolution technology for digestive endoscopic images. *Heliyon*, 10(19).

Charles Eugenio McCafferty, Marra Jai Aghajani, David Abi-Hanna, Iain Bruce Gosbell, and Slade Owen Jensen. 2018. An update on gastrointestinal endoscopy-associated infections and their contributing factors. *Annals of clinical microbiology and antimicrobials*, 17(1):36.

Sidra Naseem, Rashid Jahangir, Nazik Alturki, Faheem Shehzad, and Muhammad Sami Ullah. 2025. Deepneck: Bottleneck assisted customized deep convolutional neural networks for diagnosing gastrointestinal tract disease. *CMES - Computer Modeling in Engineering and Sciences*, 145(2):2481–2501.

Rashed Nawaz, Neelum Khalid, Fatima Ajmal, Mohammad Fazel Akbary, Shaoqing Gong, and Zhongliang Zhou. 2025. The nexus between healthcare provider distribution and neonatal mortality based on the context of maternal and child healthcare services in pakistan. *Journal of Health, Population and Nutrition*, 44(1):219.

Javeria Naz, Muhammad Attique Khan, Majed Alhaisoni, Usman Tariq, Seifedine Kadry, and 1 others. 2021. Segmentation and classification of stomach abnormalities using deep learning. *Computers, Materials & Continua*, 69(1).

OpenAI. 2023. Gpt-4 technical report. *arXiv preprint arXiv:2303.08774*.

Guilherme Penedo and 1 others. 2023. Falcon-40b: An open large language model. *ArXiv*.

Konstantin Pogorelov, Kristin Ranheim Randel, Carsten Griwodz, Sigrun Losada Eskeland, Thomas de Lange, Dag Johansen, Concetto Spampinato, Duc-Tien Dang-Nguyen, Mathias Lux, Peter Thelin Schmidt, Michael Riegler, and Pål Halvorsen. 2017. Kvasir: A multi-class image dataset for computer aided gastrointestinal disease detection. In *Proceedings of the 8th ACM on Multimedia Systems Conference*, MMSys'17, pages 164–169, New York, NY, USA. ACM.

M. Reid and 1 others. 2024. Gemini 1.5: Unlocking multimodal understanding at long context. *ArXiv*.

Paak Rewthamrongsris, Jirayu Burapacheep, Ekarat Phattarataratip, Promphakkon Kulthanaamondhita, Antonin Tichy, Falk Schwendicke, Thanaphum Osathanon, and Kraisorn Sappayatosok. 2025. Image-based diagnostic performance of llms vs cnns for oral lichen planus: Example-guided and differential diagnosis. *International Dental Journal*, 75(4):100848.

Saddaf Rubab, Muhammad Jamshed, Muhammad Attique Khan, Nouf Abdullah Almujally, Robertas Damaševičius, Amir Hussain, Neunggyu Han, and Yunyoung Nam. 2025. Gastrointestinal tract disease classification from wireless capsule endoscopy images based on deep learning information fusion and newton raphson controlled marine predator algorithm. *Scientific Reports*, 15(1):32180.

Mark Sandler, Andrew Howard, Menglong Zhu, Andrey Zhmoginov, and Liang-Chieh Chen. 2018. Mobilenetv2: Inverted residuals and linear bottlenecks. In *IEEE Conference on Computer Vision and Pattern Recognition*, pages 4510–4520.

Souvika Sarkar, Md Najib Hasan, and Santu Karmaker. 2025. Zero-shot multi-label classification of bangla documents: Large decoders vs. classic encoders. *arXiv preprint arXiv:2503.02993*.

Abdullah Şener and Burhan Ergen. 2025. Automatic detection of gastrointestinal system abnormalities using deep learning-based segmentation and classification methods. *Health Information Science and Systems*, 13(1):37.

Sourav Basak Shuvo and Mostafa Zaman Chowdhury. 2024. Classification of gallbladder cancer using average ensemble learning. In *2024 6th International Conference on Electrical Engineering and Information & Communication Technology (ICEEICT)*, pages 1450–1455. IEEE.

Samra Siddiqui, Junaid A. Khan, Tallha Akram, Meshal Alharbi, Jaehyuk Cha, and Dina A. AlHammadi. 2025. Snet: A novel convolutional neural network architecture for advanced endoscopic image classification of gastrointestinal disorders. *SLAS Technology*, 33:100304.

Karen Simonyan and Andrew Zisserman. 2015. Very deep convolutional networks for large-scale image recognition. In *International Conference on Learning Representations*.

DCEG Staff. 2020. Gastrointestinal Cancers Global Burden — dceg.cancer.gov. https://dceg.cancer.gov/news-events/news/2020/global-burden-gastro. [Accessed 12-10-2025].

Rui Su and Bingmei Liu. 2025. Computer-aided gastrointestinal disease analysis based on artificial intelligence method. *International Journal of Cognitive Informatics and Natural Intelligence*, 19(1).

Christian Szegedy, Sergey Ioffe, Vincent Vanhoucke, and Alexander Alemi. 2017. Inception-v4, inception-resnet and the impact of residual connections on learning. *AAAI Conference on Artificial Intelligence*.

Christian Szegedy, Vincent Vanhoucke, Sergey Ioffe, Jonathon Shlens, and Zbigniew Wojna. 2016. Rethinking the inception architecture for computer vision. In *IEEE Conference on Computer Vision and Pattern Recognition*, pages 2818–2826.

Mingxing Tan and Quoc Le. 2021. Efficientnetv2: Smaller models and faster training. In *International Conference on Machine Learning*, pages 10096–10106.

Mingxing Tan and Quoc V Le. 2019. Efficientnet: Rethinking model scaling for convolutional neural networks. In *International Conference on Machine Learning*, pages 6105–6114.

Gemini Team. 2024a. Gemini 2.0: Scaling multimodal understanding. *ArXiv*.

Gemma Team. 2024b. Gemma 2: Improving open language models at a practical scale. *ArXiv*.

Qwen Team. 2025. Qwen3 technical report. *ArXiv*.

Peter Valentin Tomazic, Fabian Sommer, Andreas Treccosti, Hans Rudolf Briner, and Andreas Leunig. 2021. 3d endoscopy shows enhanced anatomical details and depth perception vs 2d: a multicentre study. *European Archives of Oto-Rhino-Laryngology*, 278(7):2321–2326.

Jingpu Wang, Cas de Jongh, Zhouqiao Wu, Eline M de Groot, Sheraz R Markar, Hylke JF Brenkman, Richard van Hillegersberg, Jelle P Ruurda, and 1 others. 2025. Impact of pre-treatment waiting intervals on short-term postoperative outcomes in neoadjuvant chemotherapy followed by gastrectomy: A population-based study using the dutch upper gastrointestinal cancer audit (duca) data. *European Journal of Surgical Oncology*, page 109595.

Yan Wang, Fa Yang, Xiaoying Pan, Hao Wang, Xiaopan Xu, Yiran Pan, Kun Yang, Ge Ma, Zhangchao Hao, Huanxiang Liu, and 1 others. 2026. Improving uneven exposure using color characteristics as a priori information in endoscopic images. *Biomedical Signal Processing and Control*, 112:108825.

Wanqing Xie, Jing Hu, Pengcheng Liang, Qiao Mei, Aodi Wang, Qiuyuan Liu, Xiaofeng Liu, Juan Wu, Xiaodong Yang, Nannan Zhu, and 1 others. 2024. Deep learning–based lesion detection and severity grading of small-bowel crohn's disease ulcers on double-balloon endoscopy images. *Gastrointestinal Endoscopy*, 99(5):767–777.

Fazilet Yilmaz, Arlen Brickman, Fedaa Najdawi, Evgeny Yakirevich, Robert Egger, and Murray B Resnick. 2024. Advancing artificial intelligence integration into the pathology workflow: Exploring opportunities in gastrointestinal tract biopsies. *Laboratory Investigation*, 104(5):102043.

Shao-xiong Zeng, Qing-tian Luo, Han-lin Chen, Ji-yong Zan, and Chun-sheng Cheng. 2024. Successful diagnosis by capsule endoscopy of small intestinal ascariasis that had been misdiagnosed repeatedly. *Gastrointestinal Endoscopy*, 99(5):856–858.

Table 9: Multiple-choice performance of fifteen LLMs across four levels of prompts

Model	Class	Prompt 1			Prompt 2			Prompt 3			Prompt 4		
		Acc	F1	Kappa	Acc	F1	Kappa	Acc	F1	Kappa	Acc	F1	Kappa
GPT 4.1	Polyps	0.9600	0.8916	0.9219	0.9500	0.8527	0.9028	0.9700	0.9545	0.9415	0.9700	0.9545	0.9415
	Ulcerative Colitis	0.9800	0.7929	0.9672	0.9800	0.9000	0.9671	0.9600	0.4869	0.9346	0.9500	0.4158	0.9189
	Esophagitis	1.0000	1.0000	1.0000	1.0000	1.0000	1.0000	0.9900	0.7989	0.9483	1.0000	1.0000	1.0000
	Healthy Class	1.0000	1.0000	1.0000	1.0000	1.0000	1.0000	1.0000	1.0000	1.0000	1.0000	1.0000	1.0000
	Removal of Lesions	1.0000	1.0000	1.0000	1.0000	1.0000	1.0000	1.0000	1.0000	1.0000	1.0000	1.0000	1.0000
GPT 3.5 turbo	Polyps	0.8600	0.6976	0.7126	0.8900	0.7833	0.7814	0.8800	0.7518	0.7490	0.8800	0.5972	0.7551
	Ulcerative Colitis	0.9500	0.9497	0.9180	0.9400	0.9383	0.9022	0.9400	0.6912	0.9014	0.9300	0.7002	0.8846
	Esophagitis	1.0000	1.0000	1.0000	0.9900	0.8974	0.9460	0.9800	0.9556	0.8810	0.9700	0.7056	0.8214
	Healthy Class	1.0000	1.0000	1.0000	1.0000	1.0000	1.0000	1.0000	1.0000	1.0000	1.0000	1.0000	1.0000
	Removal of Lesions	1.0000	1.0000	1.0000	1.0000	1.0000	1.0000	0.9600	0.4898	1.0000	1.0000	1.0000	1.0000
GPT 4.1 Mini	Polyps	0.9600	0.9058	0.9212	0.9500	0.8858	0.9018	0.9500	0.8648	0.9013	0.9600	0.8828	0.9208
	Ulcerative Colitis	0.9800	0.9000	0.9671	0.9800	0.9000	0.9671	0.9800	0.9000	0.9671	0.9800	0.9000	0.9671
	Esophagitis	0.9900	0.8974	0.9460	0.9900	0.8974	0.9460	0.9800	0.8736	0.8869	0.9900	0.9794	0.9433
	Healthy Class	0.9600	0.5486	0.4872	0.9800	0.8282	0.6575	1.0000	1.0000	1.0000	1.0000	1.0000	1.0000
	Removal of Lesions	1.0000	1.0000	1.0000	1.0000	1.0000	1.0000	1.0000	1.0000	1.0000	1.0000	1.0000	1.0000
GPT 4.1 Nano	Polyps	0.9400	0.8850	0.8812	0.9500	0.9265	0.9006	0.9400	0.8708	0.8832	0.9600	0.9397	0.9228
	Ulcerative Colitis	0.9600	0.8498	0.9347	0.9500	0.8440	0.9183	0.9500	0.8217	0.9189	0.9600	0.8425	0.9349
	Esophagitis	1.0000	1.0000	1.0000	0.9900	0.9794	0.9433	0.9900	0.9794	0.9433	0.9900	0.9794	0.9433
	Healthy Class	0.9800	0.8282	0.6575	1.0000	1.0000	1.0000	0.9800	0.8282	0.6575	0.9800	0.8282	0.6575
	Removal of Lesions	1.0000	1.0000	1.0000	1.0000	1.0000	1.0000	1.0000	1.0000	1.0000	1.0000	1.0000	1.0000
O3	Polyps	0.9400	0.8330	0.8839	0.9500	0.8399	0.9025	0.9400	0.8142	0.8826	0.9700	0.9162	0.9409
	Ulcerative Colitis	0.9700	0.7234	0.9505	0.9600	0.7177	0.9341	0.9700	0.8943	0.9506	0.9900	0.9942	0.9835
	Esophagitis	0.9900	0.8974	0.9460	0.9900	0.8974	0.9460	0.9700	0.8222	0.8384	0.9900	0.8974	0.9460
	Healthy Class	1.0000	1.0000	1.0000	1.0000	1.0000	1.0000	1.0000	1.0000	1.0000	1.0000	1.0000	1.0000
	Removal of Lesions	1.0000	1.0000	1.0000	1.0000	1.0000	1.0000	1.0000	1.0000	1.0000	1.0000	1.0000	1.0000
O4-Mini	Polyps	0.9700	0.8616	0.9413	0.9600	0.8543	0.9211	0.9700	0.9068	0.9417	0.9700	0.9471	0.9406
	Ulcerative Colitis	0.9800	0.7342	0.9670	0.9700	0.8943	0.9506	0.9800	0.9000	0.9671	0.9800	0.9807	0.9668
	Esophagitis	0.9800	0.8460	0.8969	0.9700	0.8222	0.8384	0.9700	0.8562	0.8380	0.9800	0.8736	0.8869
	Healthy Class	1.0000	1.0000	1.0000	1.0000	1.0000	1.0000	1.0000	1.0000	1.0000	1.0000	1.0000	1.0000
	Removal of Lesions	1.0000	1.0000	1.0000	1.0000	1.0000	1.0000	1.0000	1.0000	1.0000	1.0000	1.0000	1.0000
O3-Mini	Polyps	0.9700	0.8988	0.9419	0.9700	0.8988	0.9419	0.9700	0.8988	0.9419	0.9600	0.8916	0.9219
	Ulcerative Colitis	0.9800	0.9000	0.9671	0.9800	0.9000	0.9671	0.9700	0.8556	0.9510	0.9800	0.9804	0.9668
	Esophagitis	0.9900	0.8974	0.9460	0.9900	0.8974	0.9460	0.9800	0.8736	0.8869	0.9800	0.8736	0.8869
	Healthy Class	1.0000	1.0000	1.0000	1.0000	1.0000	1.0000	1.0000	1.0000	1.0000	1.0000	1.0000	1.0000
	Removal of Lesions	1.0000	1.0000	1.0000	1.0000	1.0000	1.0000	1.0000	1.0000	1.0000	1.0000	1.0000	1.0000
Gemini 1.5 Flash	Polyps	0.9100	0.7899	0.8239	0.8900	0.7527	0.7847	0.9100	0.7899	0.8239	0.9200	0.8495	0.8436
	Ulcerative Colitis	0.9600	0.8498	0.9346	0.9600	0.8811	0.9344	0.9700	0.8940	0.9506	0.9700	0.8943	0.9506
	Esophagitis	0.9900	0.9794	0.9433	0.9900	0.9794	0.9433	0.9900	0.8974	0.9460	0.9800	0.8736	0.8869
	Healthy Class	1.0000	1.0000	1.0000	1.0000	1.0000	1.0000	1.0000	1.0000	1.0000	1.0000	1.0000	1.0000
	Removal of Lesions	1.0000	1.0000	1.0000	1.0000	1.0000	1.0000	1.0000	1.0000	1.0000	1.0000	1.0000	1.0000

Table 10: Multiple-choice performance of fifteen LLMs across four levels of prompts (Continued)

Model	Class	Prompt 1			Prompt 2			Prompt 3			Prompt 4		
		Acc	F1	Kappa	Acc	F1	Kappa	Acc	F1	Kappa	Acc	F1	Kappa
Gemini 1.5 Pro	Polyps	0.9200	0.8021	0.8415	0.9400	0.8295	0.8829	0.9200	0.7910	0.8412	0.9100	0.7681	0.8219
	Ulcerative Colitis	0.9800	0.9804	0.9668	0.9900	0.9942	0.9835	0.9700	0.8943	0.9506	0.9700	0.9677	0.9505
	Esophagitis	1.0000	1.0000	1.0000	0.9900	0.9794	0.9433	0.9900	0.9794	0.9433	0.9900	0.9794	0.9433
	Healthy Class	1.0000	1.0000	1.0000	1.0000	1.0000	1.0000	1.0000	1.0000	1.0000	1.0000	1.0000	1.0000
	Removal of Lesions	1.0000	1.0000	1.0000	1.0000	1.0000	1.0000	1.0000	1.0000	1.0000	1.0000	1.0000	1.0000
Gemini 1.5 Flash 8b	Polyps	0.8100	0.6430	0.5716	0.8000	0.5914	0.5432	0.7900	0.5162	0.5021	0.7900	0.5177	0.5088
	Ulcerative Colitis	0.9600	0.7221	0.9333	0.9200	0.8468	0.8671	0.9200	0.9036	0.8649	0.8900	0.8724	0.8133
	Esophagitis	0.9800	0.9556	0.8810	0.9800	0.9615	0.8917	0.9600	0.8431	0.7349	0.9700	0.8709	0.8116
	Healthy Class	1.0000	1.0000	1.0000	1.0000	1.0000	1.0000	1.0000	1.0000	1.0000	1.0000	1.0000	1.0000
	Removal of Lesions	1.0000	1.0000	1.0000	1.0000	1.0000	1.0000	1.0000	1.0000	1.0000	1.0000	1.0000	1.0000
Gemini 2.0 Flash	Polyps	0.9300	0.8199	0.8592	0.9300	0.8678	0.8602	0.9400	0.8746	1.0000	0.9500	0.8842	0.9016
	Ulcerative Colitis	0.9700	0.8556	0.9510	0.9700	0.7234	0.9505	0.9700	0.8873	0.9509	0.9400	0.6573	0.9040
	Esophagitis	0.9900	0.9794	0.9433	0.9900	0.9794	0.9433	0.9900	0.9794	0.9433	0.9800	0.7824	0.8921
	Healthy Class	1.0000	1.0000	1.0000	1.0000	1.0000	1.0000	1.0000	1.0000	1.0000	0.9800	0.8282	0.6575
	Removal of Lesions	1.0000	1.0000	1.0000	1.0000	1.0000	1.0000	1.0000	1.0000	1.0000	1.0000	1.0000	1.0000
Tiiuae/Falcon3 7b Base	Polyps	0.5100	0.3691	0.3037	0.6700	0.4438	0.4697	0.3900	0.2366	0.1782	0.3600	0.1843	0.1160
	Ulcerative Colitis	0.5800	0.4178	0.4239	0.8000	0.5542	0.6960	0.3300	0.3271	0.2026	0.2700	0.1810	0.0982
	Esophagitis	0.4700	0.2096	0.0908	0.8000	0.4807	0.4331	0.3800	0.2097	0.0975	0.3100	0.1737	0.0483
	Healthy Class	0.6400	0.1580	0.0333	0.7200	0.1694	0.0463	0.4600	0.2799	0.0486	0.2600	0.0839	0.0043
	Removal of Lesions	0.4400	0.1528	0.0000	0.6400	0.1561	0.0000	0.3600	0.1324	0.0000	0.4800	0.1622	0.0000
Ministral 8B	Polyps	0.1900	0.2550	0.0810	0.5300	0.5276	0.3369	0.5100	0.3411	0.2326	0.6600	0.3860	0.3665
	Ulcerative Colitis	0.4200	0.5299	0.2926	0.4900	0.5675	0.3526	0.5400	0.3719	0.3711	0.7400	0.5593	0.6084
	Esophagitis	0.3500	0.3101	0.0714	0.5000	0.3476	0.0871	0.6000	0.2264	0.1063	0.8400	0.6167	0.4554
	Healthy Class	0.2400	0.1311	0.0058	0.4000	0.5196	0.0434	0.5800	0.5758	0.0683	0.7400	0.3784	0.1144
	Removal of Lesions	0.2800	0.2188	0.0000	0.2000	0.1111	0.0000	0.4400	0.2037	0.0000	0.6000	0.3750	0.0000
Meta Lama 3.2	Polyps	0.3100	0.1988	0.0556	0.6000	0.3947	0.3398	0.6200	0.3527	0.3513	0.6300	0.3104	0.3534
	Ulcerative Colitis	0.3200	0.2134	0.0969	0.6100	0.4468	0.4404	0.6900	0.5060	0.5502	0.5500	0.3607	0.3548
	Esophagitis	0.3600	0.1859	0.0698	0.5600	0.2422	0.1240	0.7700	0.3886	0.3328	0.6600	0.2760	0.1764
	Healthy Class	0.3400	0.1030	0.0030	0.4200	0.1604	0.0410	0.7200	0.2917	0.1026	0.7000	0.1647	-0.0218
	Removal of Lesions	0.4800	0.1622	0.0000	0.7200	0.1674	0.0000	0.5600	0.1436	0.0000	0.6400	0.1561	0.0000
Qwen3-14B	Polyps	0.2000	0.1578	0.0741	0.2900	0.2500	0.1419	0.2200	0.1714	0.1079	0.2900	0.2656	0.1539
	Ulcerative Colitis	0.3400	0.2836	0.2272	0.3400	0.3498	0.2384	0.1500	0.1374	0.0818	0.2400	0.2174	0.1566
	Esophagitis	0.4800	0.2933	0.1224	0.4400	0.4253	0.1223	0.2600	0.2417	0.0729	0.3000	0.3145	0.0727
	Healthy Class	0.4400	0.1549	0.0155	0.4400	0.4000	0.0476	0.2000	0.0678	0.0050	0.2000	0.0678	0.0045
	Removal of Lesions	0.6400	0.1951	0.0000	0.5600	0.1795	0.0000	0.3600	0.1765	0.0000	0.5200	0.2281	0.0000

Table 11: Reasoning performance of fifteen LLMs across four levels of prompts

Model	Class	Prompt 1			Prompt 2			Prompt 3			Prompt 4		
		BERT	Cosine	Rouge	BERT	Cosine	Rouge	BERT	Cosine	Rouge	BERT	Cosine	Rouge
GPT 4.1	Polyps	0.9006	0.4117	0.2840	0.8919	0.4055	0.2535	0.8962	0.4053	0.2690	0.8944	0.4095	0.2620
	Ulcerative Colitis	0.8968	0.4232	0.2698	0.8894	0.4136	0.2487	0.8923	0.4155	0.2639	0.8855	0.4047	0.2342
	Esophagitis	0.8951	0.4041	0.2620	0.8805	0.3599	0.2182	0.8907	0.3918	0.2503	0.8848	0.3822	0.2299
	Healthy Class	0.8818	0.5269	0.2926	0.8836	0.5546	0.3092	0.8593	0.4630	0.2416	0.8666	0.4901	0.2467
	Removal of Lesions	0.8736	0.3975	0.2407	0.8779	0.3989	0.2391	0.8652	0.3752	0.2254	0.8768	0.4109	0.2548
GPT 3.5 turbo	Polyps	0.8923	0.3364	0.2512	0.8994	0.3700	0.2749	0.8656	0.3074	0.1935	0.8778	0.3481	0.2346
	Ulcerative Colitis	0.8958	0.3921	0.2678	0.8963	0.3875	0.2718	0.8642	0.3249	0.1942	0.8776	0.3619	0.2350
	Esophagitis	0.8968	0.3772	0.2742	0.8968	0.3782	0.2634	0.8718	0.3391	0.2141	0.8827	0.3681	0.2374
	Healthy Class	0.8211	0.1904	0.1092	0.8265	0.2057	0.1125	0.8694	0.4874	0.2472	0.8609	0.4435	0.2252
	Removal of Lesions	0.8564	0.2867	0.1909	0.8399	0.2140	0.1361	0.8639	0.3435	0.2175	0.8616	0.3639	0.2239
GPT 4.1 Mini	Polyps	0.8944	0.4130	0.2751	0.8918	0.3998	0.2726	0.8731	0.3335	0.2263	0.8615	0.3034	0.1902
	Ulcerative Colitis	0.8944	0.4130	0.2751	0.8918	0.3998	0.2726	0.8731	0.3335	0.2263	0.8615	0.3034	0.1902
	Esophagitis	0.9065	0.4016	0.2600	0.9004	0.3885	0.2405	0.8738	0.3137	0.2050	0.8661	0.3420	0.1945
	Healthy Class	0.8802	0.4782	0.2603	0.8868	0.4869	0.2738	0.8721	0.4390	0.2371	0.8565	0.4879	0.2125
	Removal of Lesions	0.8890	0.4020	0.2459	0.8895	0.3945	0.2394	0.8712	0.3640	0.2191	0.8722	0.3765	0.2332
GPT 4.1 Nano	Polyps	0.8737	0.3278	0.2141	0.8880	0.3780	0.2508	0.8819	0.3599	0.2296	0.8655	0.3186	0.1960
	Ulcerative Colitis	0.8674	0.3124	0.1886	0.8926	0.3812	0.2436	0.8844	0.3817	0.2285	0.8725	0.3641	0.2070
	Esophagitis	0.8819	0.3394	0.2210	0.8948	0.3704	0.2405	0.8908	0.3915	0.2388	0.8791	0.3897	0.2222
	Healthy Class	0.8330	0.3323	0.1563	0.8440	0.3470	0.1693	0.8661	0.4686	0.2395	0.8644	0.5070	0.2320
	Removal of Lesions	0.8229	0.1735	0.0853	0.8292	0.2004	0.1011	0.8572	0.3416	0.1986	0.8611	0.3724	0.2072
O3	Polyps	0.8688	0.3231	0.2021	0.8665	0.3136	0.1936	0.8649	0.3034	0.1897	0.8702	0.3221	0.2040
	Ulcerative Colitis	0.8777	0.3115	0.1888	0.8742	0.3040	0.1855	0.8705	0.2928	0.1799	0.8780	0.3029	0.1831
	Esophagitis	0.8826	0.3097	0.1985	0.8746	0.3002	0.1855	0.8780	0.3060	0.1884	0.8818	0.3070	0.1991
	Healthy Class	0.8558	0.3898	0.1913	0.8621	0.4006	0.2004	0.8555	0.3895	0.1965	0.8639	0.4251	0.2169
	Removal of Lesions	0.8635	0.2930	0.1665	0.8698	0.3191	0.1736	0.8655	0.3213	0.1816	0.8737	0.3357	0.1975
O4-Mini	Polyps	0.8735	0.2923	0.2148	0.8733	0.2890	0.2168	0.8650	0.2659	0.1993	0.7817	0.0000	0.0000
	Ulcerative Colitis	0.8852	0.2766	0.2077	0.8825	0.2823	0.1980	0.8749	0.2540	0.1896	0.7791	0.0000	0.0000
	Esophagitis	0.8832	0.2654	0.2031	0.8845	0.2832	0.2047	0.8780	0.2639	0.1961	0.8832	0.2790	0.2034
	Healthy Class	0.8608	0.3267	0.1911	0.8650	0.3525	0.1976	0.8679	0.3704	0.2119	0.7779	0.0000	0.0000
	Removal of Lesions	0.8652	0.2690	0.1821	0.8614	0.2686	0.1709	0.8669	0.2705	0.1905	0.7842	0.0000	0.0000

Table 12: Reasoning performance of fifteen LLMs across four levels of prompts (continued)

Model	Class	Prompt 1			Prompt 2			Prompt 3			Prompt 4		
		BERT	Cosine	Rouge	BERT	Cosine	Rouge	BERT	Cosine	Rouge	BERT	Cosine	Rouge
O3-Mini	Polyps	0.7817	0.0000	0.0000	0.7817	0.0000	0.0000	0.7817	0.0000	0.0000	0.7817	0.0000	0.0000
	Ulcerative Colitis	0.7791	0.0000	0.0000	0.7791	0.0000	0.0000	0.7791	0.0000	0.0000	0.7791	0.0000	0.0000
	Esophagitis	0.7763	0.0000	0.0000	0.7763	0.0000	0.0000	0.7763	0.0000	0.0000	0.7763	0.0000	0.0000
	Healthy Class	0.7779	0.0000	0.0000	0.7779	0.0000	0.0000	0.7779	0.0000	0.0000	0.7779	0.0000	0.0000
	Removal of Lesions	0.7842	0.0000	0.0000	0.7842	0.0000	0.0000	0.7842	0.0000	0.0000	0.7842	0.0000	0.0000
Gemini 1.5 Flash	Polyps	0.8588	0.2684	0.1887	0.8711	0.3242	0.2212	0.8706	0.3240	0.2121	0.8660	0.2951	0.1989
	Ulcerative Colitis	0.8620	0.2655	0.1747	0.8839	0.3552	0.2226	0.8837	0.3629	0.2285	0.8882	0.3685	0.2358
	Esophagitis	0.8584	0.2584	0.1705	0.8836	0.3332	0.2163	0.8834	0.3307	0.2203	0.8861	0.3480	0.2280
	Healthy Class	0.8294	0.3071	0.1516	0.8340	0.3169	0.1538	0.8348	0.3667	0.1705	0.8556	0.4248	0.2110
	Removal of Lesions	0.8424	0.2702	0.1509	0.8444	0.2904	0.1515	0.8666	0.3290	0.2017	0.8622	0.3348	0.2093
Gemini 1.5 Pro	Polyps	0.8424	0.2702	0.1509	0.8444	0.2904	0.1515	0.8666	0.3290	0.2017	0.8622	0.3348	0.2093
	Ulcerative Colitis	0.8775	0.3597	0.2227	0.8752	0.3685	0.2067	0.8865	0.4078	0.2343	0.8793	0.3572	0.2191
	Esophagitis	0.8705	0.3208	0.1944	0.8714	0.3312	0.2041	0.8874	0.3968	0.2368	0.8839	0.3636	0.2280
	Healthy Class	0.8705	0.3208	0.1944	0.8714	0.3312	0.2041	0.8874	0.3968	0.2368	0.8839	0.3636	0.2280
	Removal of Lesions	0.8412	0.2411	0.1361	0.8381	0.2107	0.1203	0.8541	0.3678	0.1850	0.8652	0.3225	0.2086
Gemini 1.5 Flash 8b	Polyps	0.8811	0.3011	0.2323	0.8795	0.3114	0.2274	0.8624	0.3067	0.1955	0.8657	0.3063	0.2051
	Ulcerative Colitis	0.8860	0.3300	0.2269	0.8893	0.3647	0.2248	0.8770	0.3543	0.2108	0.8834	0.3673	0.2299
	Esophagitis	0.8826	0.2938	0.2137	0.8851	0.3267	0.2161	0.8723	0.3132	0.1999	0.8778	0.3397	0.2102
	Healthy Class	0.8460	0.3685	0.1860	0.8441	0.4101	0.1881	0.8542	0.4170	0.2126	0.8626	0.4309	0.2388
	Removal of Lesions	0.8551	0.2980	0.1731	0.8548	0.3007	0.1758	0.8717	0.3602	0.2092	0.8723	0.3702	0.2178
Gemini 2.0 Flash	Polyps	0.8815	0.3204	0.2351	0.8732	0.3216	0.2143	0.8626	0.3170	0.2015	0.8512	0.2769	0.1804
	Ulcerative Colitis	0.8836	0.3604	0.2396	0.8849	0.3811	0.2325	0.8754	0.3817	0.2140	0.8541	0.2862	0.1805
	Esophagitis	0.8785	0.3027	0.2085	0.8841	0.3609	0.2259	0.8700	0.3477	0.2060	0.8547	0.2814	0.1778
	Healthy Class	0.8342	0.3122	0.1667	0.8333	0.3084	0.1607	0.8453	0.4189	0.2101	0.8423	0.4014	0.2009
	Removal of Lesions	0.8458	0.2451	0.1526	0.8553	0.3485	0.1795	0.8578	0.3491	0.2035	0.8582	0.3599	0.2098